Effects of self-consistency in a Green's function description of saturation in nuclear matter

Y. Dewulf, D. Van Neck, and M. Waroquier
Laboratory of Theoretical Physics, Ghent University, Proeftuinstraat 86, B-9000 Gent, Belgium
(Received 16 January 2002; published 9 May 2002)

The binding energy in nuclear matter is evaluated within the framework of self-consistent Green's function theory, using a realistic nucleon-nucleon interaction. The two-body dynamics is solved at the level of summing particle-particle and hole-hole ladders. We go beyond the on-shell approximation and use intermediary propagators with a discrete-pole structure. A three-pole approximation is used, which provides a good representation of the quasiparticle excitations, as well as reproducing the zeroth- and first-order energy-weighted moments in both the nucleon removal and addition domains of the spectral function. Results for the binding energy are practically independent of the details of the discretization scheme. The main effect of the increased self-consistency is to introduce an additional density dependence, which causes a shift towards lower densities and smaller binding energies, as compared to a (continuous choice) Brueckner calculation with the same interaction. Particle number conservation and the Hugenholz–Van Hove theorem are satisfied with reasonable accuracy.

DOI: 10.1103/PhysRevC.65.054316 PACS number(s): 21.65.+f, 24.10.Cn

I. INTRODUCTION

The determination of the quantum-mechanical properties of many-body systems in a fully microscopic way is an important challenge in physics. For many systems, such as atoms and molecules, an average treatment of the medium effects by means of a Hartree-Fock (HF) field already leads to reasonable results. This is not the case for nuclear systems when using realistic nucleon-nucleon (*NN*) interactions. Due to the strong repulsive core in these interactions one has to go beyond the basic mean-field treatment, since the core dominates the two-body matrix elements and leads to unbound nuclear systems in HF calculations [1,2].

The short-range correlations, originating from the repulsive core, can be accounted for in a number of ways [3]. In both the hole line expansion, of which the Brueckner-Hartree-Fock (BHF) approach corresponds to the lowest-order truncation, and the Green's function formalism, the realistic *NN* interaction is replaced by a medium-dependent effective interaction that can be calculated microscopically. Other techniques such as variational and correlated basis function (CBF) calculations replace the Slater determinant, representing the uncorrelated ground state, with a correlated many-body wave function.

The repulsive core of the interaction couples low-lying single-particle states to excitations at very high energies. Because of the difference in relevant energy scale, the effects of short-range correlations are believed to be independent of the specific low-energy shell structure of the nuclei. Therefore it is advantageous to study these short-range effects in infinite nuclear matter rather than in finite nuclei, as the symmetry of such a system considerably simplifies the calculations. Infinite nuclear matter contains equal numbers of protons and neutrons, homogeneously distributed in space. Furthermore, the Coulomb interaction between the protons is neglected. Due to translational invariance, plane waves constitute a suitable single-particle basis for the calculations. The uncorrelated ground state then corresponds to a Slater determinant with all momenta occupied up to the Fermi momentum.

Although an idealized system, some experimental data are available for nuclear matter. Its binding energy in principle corresponds to the volume term, $a_V = 16$ MeV, in the Bethe–von Weizsacker formula [4,5], since the surface, Coulomb, and asymmetry contributions are absent. The saturation density of nuclear matter can be deduced from the central density of heavy nuclei and corresponds to a density of about $0.17\ \mathrm{fm}^{-3}$, or a Fermi momentum of $k_F = 1.36\ \mathrm{fm}^{-1}$.

Nonrelativistic many-body calculations using only two-body interactions have been unable to reproduce this empirical saturation point. BHF calculations performed for various *NN* interactions lead to different saturation points. This reflects the fact that all modern potentials have been fitted to the binding energy of the deuteron and *NN* scattering data up to a certain energy, but give very different results when used to describe many-body systems. However, the different saturation points are all located on a line in the binding energy versus density plot, the Coester line [6], which does not meet the empirical saturation point. Some potentials saturate at the correct density, but are underbound, while others predict the correct binding energy but at too high densities. Furthermore, for the same potential, BHF results differ from variational calculations [7]. The reason for the latter discrepancy can be found in the fact that the BHF approximation corresponds to the lowest-order term in the hole-line expansion. In the BHF approach the effective interaction is calculated by summing all particle-particle ladder diagrams. Neglecting hole-hole propagation might be valid for low densities, as the phase space for hole-hole propagation is then much smaller than for particle-particle propagation, but at larger densities higher orders in the hole lines should be included. Calculations including three-hole line contributions [8] agree reasonably well with advanced variational results [9,10] and shift the saturation point off the Coester line. However, the shift is still not large enough for a reproduction of the empirical point.

Both a relativistic extension of the theory (Dirac-Brueckner approach [11]), and the incorporation of three-

body interactions [10,12], that can in part be linked to Δ degrees of freedom, lead to a correct saturation point. However, both extensions contain phenomenological ingredients to some extent and do not correctly describe all aspects of the many-body system. More work needs to be done in order to clarify the saturation properties of nuclear matter. At the same time there is another mechanism that deserves a more profound study: a *self-consistent* treatment of short-range correlations.

The BHF approach is essentially an independent particle model (IPM), in which each particle moves through the medium with a specific energy determined by its momentum. The Fermi sea is completely filled up to the Fermi momentum: hole states have an occupation probability of unity, while particle states are completely unoccupied. The validity of this approximation was investigated in $(e,e'p)$ knockout experiments [13]. These experiments show considerable broadening of the hole strength distributions as one moves away from the Fermi surface, corresponding to a finite lifetime of the quasiparticle excitations. The same experiments indicate that the hole states are considerably depleted. This depletion is most pronounced for states close to the Fermi surface. Using the CERES method [14] an occupation number of 0.75 has been obtained for the $3s_{1/2}$ orbital in ^{208}Pb [15]. There is thus clear experimental evidence for a Fermi sea strongly deformed by nuclear correlations. Projection operators that are used in the calculation of the effective interaction should be defined with respect to this deformed Fermi sea, rather than the uncorrelated one. This introduces an additional density dependence in the saturation mechanism that may shift the saturation point off the Coester line.

The above discussion is naturally related to the concept of self-consistent Green's function (SCGF) approaches. The binding energy, as well as all single-particle observables, can be calculated from the exact single-particle propagator dressed by the medium. The dressed propagator is obtained from the Dyson equation, where the irreducible self-energy accounts for the medium effects. This self-energy is obtained from an expansion in terms of the effective interaction, which corresponds to the sum of all ladder diagrams. In contrast to the Brueckner approach, particle-particle (pp) and hole-hole (hh) ladders are treated in a completely symmetrical way, so that the Green's function scheme is also suited for calculations at larger densities. Self-consistency now demands that the dressed Green's function, which is obtained from the Dyson equation, is also used in the evaluation of the self-energy and the effective interaction.

Self-consistency is a crucial ingredient for the fulfillment of a number of sum rules, such as the conservation of particle number [16]. Usually a self-consistent solution is obtained by means of an iterative approach, but it is not at all easy to calculate the effective interaction with completely dressed Green's functions. The corresponding dressed spectral functions show a complicated energy dependence, containing both sharp peaks (reflecting the quasiparticle behavior) and a broad background distribution, absent in IPM calculations.

In the past several SCGF calculations have been performed using various approximations to the spectral function, both for $T=0$ and $T\neq 0$. At finite temperatures calculations are somewhat easier, as the quasiparticle peaks acquire a considerable width, due to thermal broadening, even close to the Fermi momentum. An overview of the off-shell effects for a separable model interaction and $T\neq 0$ is presented in Ref. [17].

Another important issue arising in self-consistent calculations is the appearance of pairing instabilities. These are a result of the inclusion of hh propagation in the effective interaction [18], and manifest themselves as complex poles in the effective interaction. Pairing correlations are very sensitive to the occupation probability of states around the Fermi surface. As short-range correlations tend to modify this Fermi surface, they weaken the pairing correlations. When performing fully self-consistent calculations the deformation of the Fermi surface is taken into account in the definition of the effective interaction, and it turns out that the pairing instabilities are removed at densities close to the empirical saturation density.

Only recently were results obtained for realistic potentials including the correct off-shell behavior of nucleons for $T=0$. These calculations employed a parametrized spectral function [19,20]. In this paper an alternative approach is followed, using a discrete multiple-pole representation of the spectral function. From a numerical point of view, this approximation basically corresponds to an extension of the quasiparticle approach, which has some computational advantages.

The outline of this paper is as follows. In Sec. II the basic concepts of the self-consistent Green's function framework are introduced. Section III focuses on the construction of discretization schemes for the spectral function. In Sec. IV some numerical details on the calculation of the effective interaction are presented. Section V discusses the relation of pairing correlations and modifications of the Fermi surface. The self-energy within the discrete scheme is discussed in Sec. VI. Section VII presents results for quantities such as spectral functions, occupation probabilities, and binding energy. Special attention is paid to the effects of self-consistency on the saturation properties. Finally, Sec. VIII contains a summary and conclusions. All calculations are performed using the Reid 93 interaction defined in Ref. [21].

II. FORMALISM

Plane waves constitute a suitable single-particle basis in nuclear matter because of the translational invariance. In symmetric and unpolarized nuclear matter, the one-particle Green's function is independent of spin and isospin variables and completely specified by the magnitude of the momentum $\vec{p}$ and the energy of the particle ω. In this basis the one-particle Green's function can be represented in Lehmann's representation as follows:

$$g(p,\omega)=\int_{-\infty}^{\epsilon_F} d\omega' \frac{S_h(p,\omega')}{\omega-\omega'-i\eta}+\int_{\epsilon_F}^{+\infty} d\omega' \frac{S_p(p,\omega')}{\omega-\omega'+i\eta}, \tag{1}$$

where ϵ_F is the Fermi energy of the system. All information on the one-particle properties is contained in the spectral

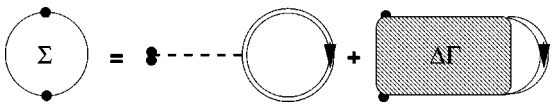

FIG. 1. Diagrammatic representation of the effective interaction in the ladder approximation. The dashed line represents the bare *NN* interaction *V*, while the $\Delta\Gamma$ box corresponds to the energy-dependent part of the effective interaction in Fig. 2. The propagators are fully dressed.

functions S_p and S_h, which also allow an intuitive interpretation of the Green's function. The particle spectral function $S_p(p,\omega)$ represents the probability of adding a particle with momentum p to the system, while leaving the resulting system with an excitation energy ω. The hole spectral function $S_h(p,\omega)$ is related in a similar way to the removal of a particle with momentum p.

For free particles the spectral function reduces to a single δ peak located at the corresponding kinetic energy,

$$S_h(p,\omega)=\theta(k_F-p)\,\delta(\omega-p^2/2m),$$

$$S_p(p,\omega)=\theta(p-k_F)\,\delta(\omega-p^2/2m). \tag{2}$$

In a correlated system the energy dependence of the spectral functions is much more complicated and can be determined by solving the Dyson equation,

$$g(p,\omega)=g_0(p,\omega)+g_0(p,\omega)\Sigma(p,\omega)g(p,\omega). \tag{3}$$

Here g_0 represents the free propagator, corresponding to the spectral functions of Eq. (2). The irreducible self-energy Σ is a complex quantity representing the interaction with the other particles of the medium. Inserting the free propagator, as well as the Lehmann representation for the fully dressed propagator (1) in the Dyson equation (3) leads to the following expressions for the dressed spectral functions:

$$S_h(p,\omega)=\begin{cases}\dfrac{1}{\pi}\dfrac{\mathrm{Im}\,\Sigma(p,\omega)}{[\omega-p^2/2m-\mathrm{Re}\,\Sigma(p,\omega)]^2+[\mathrm{Im}\,\Sigma(p,\omega)]^2} & \text{if } \omega<\epsilon_F\\ 0 & \text{if } \omega>\epsilon_F,\end{cases}$$

$$S_p(p,\omega)=\begin{cases}0 & \text{if } \omega<\epsilon_F\\ -\dfrac{1}{\pi}\dfrac{\mathrm{Im}\,\Sigma(p,\omega)}{[\omega-p^2/2m-\mathrm{Re}\,\Sigma(p,\omega)]^2+[\mathrm{Im}\,\Sigma(p,\omega)]^2} & \text{if } \omega>\epsilon_F.\end{cases} \tag{4}$$

These correlated spectral functions typically consist of a sharp peak, corresponding to the quasiparticle extension of the δ peak in the uncorrelated case, combined with a broad background in both the addition and removal domains.

The central concept in the determination of the correlated spectral function is the self-energy, obtained by summing diagrams of different orders in the interaction [16,22]. This perturbation series is usually truncated at some finite order. Retaining for instance only the first order term in the interaction corresponds to the Hartree-Fock approach.

Within the SCGF framework, short-range correlations are treated by replacing the free *NN* interaction with an effective in-medium interaction Γ, calculated from the free interaction by summing all diagrams of the ladder type (Fig. 1). In contrast to the in-medium interaction introduced by Brueckner and co-workers [23–25], Γ contains both intermediate hh and pp propagation. Its matrix elements between *NN* states with center-of-mass momentum $\vec{P}$ and relative momenta $\vec{q}$ and $\vec{q}\,'$ obeys the integral equation

$$\langle\vec{q}|\Gamma(P,\Omega)|\vec{q}\,'\rangle=\langle\vec{q}|V|\vec{q}\,'\rangle+\int\frac{d\vec{q}\,''}{(2\pi)^3}\langle\vec{q}|V|\vec{q}\,''\rangle \times\left[\int d\omega\int d\omega'\frac{S_p(p_1,\omega)S_p(p_2,\omega')}{\Omega-\omega-\omega'+i\eta}-\int d\omega\int d\omega'\frac{S_h(p_1,\omega)S_h(p_2,\omega')}{\Omega-\omega-\omega'-i\eta}\right]\langle\vec{q}\,''|\Gamma(P,\omega)|\vec{q}\,'\rangle, \tag{5}$$

where $\vec{p}_{1,2}=\vec{P}/2\pm\vec{q}\,''$. To facilitate the evaluation of the self-energy, the effective interaction Γ can be split into a part corresponding to the free *NN* interaction and an energy-dependent correction term,

$$\langle\vec{q}|\Gamma(P,\Omega)|\vec{q}\,'\rangle=\langle\vec{q}|V|\vec{q}\,'\rangle+\langle\vec{q}|\Delta\Gamma(P,\Omega)|\vec{q}\,'\rangle, \tag{6}$$

where $\Delta\Gamma$ satisfies following dispersion relation:

$$\langle\vec{q}|\Delta\Gamma(P,\Omega)|\vec{q}\,'\rangle=\frac{1}{\pi}\int_{-\infty}^{2\epsilon_F}d\Omega'\frac{\mathrm{Im}\langle\vec{q}|\Gamma(P,\Omega')|\vec{q}\,'\rangle}{\Omega-\Omega'-i\eta}-\frac{1}{\pi}\int_{2\epsilon_F}^{\infty}d\Omega'\frac{\mathrm{Im}\langle\vec{q}|\Gamma(P,\Omega')|\vec{q}\,'\rangle}{\Omega-\Omega'+i\eta}. \tag{7}$$

Retaining in the expansion for the self-energy only the first-order term in the effective interaction, one finds

$$\Sigma(p,\omega) = -\frac{i}{(2\pi)^4}\int d\vec{p}\,' d\omega' \langle \vec{q}|\Gamma(\vec{P},\omega+\omega')|\vec{q}\rangle g(\vec{p'},\omega') \tag{8}$$

where $\vec{P}=\vec{p}+\vec{p}\,'$ and $\vec{q}=(\vec{p}-\vec{p}\,')/2$. A more tractable form for the self-energy is obtained, using the Lehmann representation (1) together with the dispersion relation (7) for Γ,

$$\Sigma(p,\omega) = \int \frac{d\vec{p}\,'}{(2\pi)^3}\langle \vec{q}|V|\vec{q}\rangle \int_{-\infty}^{\epsilon_F} d\omega' S_h(p',\omega') - \int \frac{d\vec{p}\,'}{(2\pi)^3}\int_{-\infty}^{\epsilon_F} d\omega' \int_{2\epsilon_F}^{\infty} d\Omega'' \frac{\mathrm{Im}\langle \vec{q}|\Gamma(P,\Omega'')|\vec{q}\rangle}{\omega+\omega'-\Omega''+i\eta} S_h(p',\omega')$$
$$- \int \frac{d\vec{p}\,'}{(2\pi)^3}\int_{\epsilon_F}^{\infty} d\omega' \int_{-\infty}^{2\epsilon_F} d\Omega'' \frac{\mathrm{Im}\langle \vec{q}|\Gamma(P,\Omega'')|\vec{q}\rangle}{\omega+\omega'-\Omega''-i\eta} S_p(p',\omega'). \tag{9}$$

A diagrammatic representation is presented in Fig. 2, where the second diagram corresponds to both the second and third term in Eq. (9).

When one wants to satisfy important conservation laws, self-consistency becomes a crucial requirement. This means that the spectral functions used in the evaluation of the effective interaction (5) and the self-energy (9) are themselves solutions of the Dyson equation (4). As a result one needs to solve a set of coupled nonlinear equations, which is usually done by iteration. Starting from an initial guess for the Green's function (e.g., the free Green's function in the case of nuclear matter calculations), the effective interaction and the self-energy are calculated. In the next step the new spectral functions are determined from the Dyson equation and reinserted in the equations for the effective interaction and the self-energy. This procedure is repeated until the spectral function is converged.

During such an iterative process, the spectral function changes from the single δ peak to a more complicated structure. Especially at $T=0$ (zero temperature), the evaluation of the effective interaction through successive iterations turns out to be a cumbersome task when using dressed spectral functions. The very sharp peaks, combined with the broad background distribution in the spectral function make accurate numerical evaluations difficult. Therefore it is important to find a suitable approximation for the spectral function that can be used to evaluate the effective interaction and the self-energy during successive iterations. Such an approximation must allow a fast evaluation of Σ and Γ, but at the same time it must retain the most prominent features of the full spectral function. In the next section we will demonstrate how the discrete-pole approximation satisfies both needs.

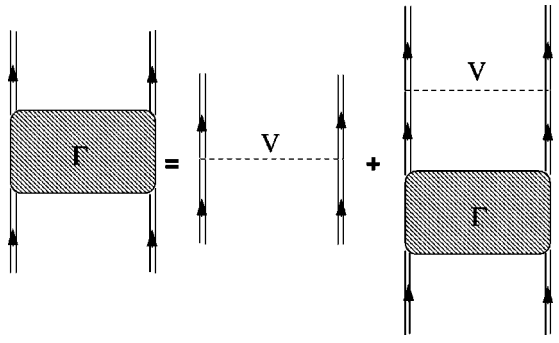

FIG. 2. Diagrammatic representation of the irreducible self-energy in nuclear matter within the present self-consistent framework.

III. DISCRETIZATION SCHEMES

In the past, several approximations to the spectral functions have been proposed, the most basic of them being the ''quasiparticle'' approximation. Within this approximation the imaginary part of the self-energy is neglected, so that the full spectral function of Eq. (4) is replaced by a single δ peak located at the ''on-shell energy,''

$$\epsilon_{\mathrm{qp}}(p) = p^2/2m + \mathrm{Re}\,\Sigma(p,\epsilon_{\mathrm{qp}}(p)). \tag{10}$$

This quasiparticle approach is similar to the continuous Brueckner-Hartree-Fock (c-BHF) prescription [26], but also includes *hh* propagation in the effective interaction. Extended calculations within this scheme have been performed for a model interaction [28]. When the quasiparticle scheme is implemented for realistic *NN* interactions (containing attractive components) one runs into trouble with pairing instabilities. The nucleons tend to form pairs, which is signaled by the appearance of complex conjugate poles in the effective interaction [27]. A way to avoid these instabilities while staying within a pure single-pole scheme was formulated by Vonderfecht *et al.* [29], who replaced the on-shell energy for hole states ($p<k_F$) by the mean removal energy. The resulting gap in the single-particle spectrum is large enough to remove the pairing instabilities even when using realistic interactions.

When going beyond the quasiparticle approximation and incorporating effects of intermediate off-shell propagation of nucleons, the complex poles in Γ may disappear. The responsible mechanism is the use of a correlated Pauli operator, instead of the uncorrelated projection operator used in a quasiparticle calculation. The width of the quasiparticle peak, as well as the broad background distribution in the spectral function, containing about 15–25 % of the total strength, is neglected within the quasiparticle approximation. This background distribution is responsible for a depletion of the hole

states and a corresponding partial occupation of the particle states, resulting in an effective reduction of the interaction strength near the Fermi surface. A more complete treatment of the many-body problem, using the full energy dependence of the spectral function, can thus remove the pairing instabilities around the empirical saturation density, as will be demonstrated in Sec. V. When constructing an approximation to the spectral function, it is therefore crucial that a realistic description of the strength distribution around the Fermi energy is incorporated.

In recent years several attempts have been made to improve on the quasiparticle scheme using an approximated spectral function that is in closer agreement with the exact spectral function. de Jong and Lenske [30] follow a mixed approach: for hole states ($p<k_F$) the complete particle spectral function ($\omega>\epsilon_F$) is retained. This particle spectral function does not contain sharp peaks and consequently does not lead to large numerical difficulties. The hole spectral function does contain a quasiparticle peak and is replaced by a single renormalized δ function. For particle states ($p>k_F$) a similar approach is followed. Although part of the background distribution is incorporated in this calculation, the deformation of the Fermi surface is insufficient to remove pairing instabilities and the calculation could only be done for a model interaction. The group of Dickhoff retains the full energy dependence of the spectral function, using a parametrization of the spectral function [19] so that most integrals can be carried out analytically. Recent research of this group seems to favor a parametrization of the self-energy instead of a parametrization of the spectral function [20].

In this paper we investigate an extension of the quasiparticle approximation that aims at incorporating the off-shell propagation of the particles in a self-consistent way. This is achieved by replacing the single pole of the quasiparticle Green's function by a set of discrete poles, each carrying a fraction of the strength,

$$g(p,\omega)=\sum_i \frac{f_i(p)}{\omega-F_i(p)+i\eta}+\sum_j \frac{b_j(p)}{\omega-B_j(p)-i\eta}. \tag{11}$$

The additional poles can be used to represent the background in both the addition and removal domains. Poles located below the Fermi energy will be labeled as B_j, poles above the Fermi energy as F_i.

A discrete representation (11) of the Green's function can be employed in an iterative procedure, similarly as in the quasiparticle approximation. Starting from an initial guess for the Green's function (e.g., the free Green's function), the self-energy and effective interaction are calculated. Instead of retaining the complete energy dependence of the spectral function according to Eq. (4), a fixed number of discrete poles, F_i, B_j, and their corresponding residues, f_i, b_j, are determined as functions of single-particle momentum. The resulting discrete Green's function is then reinserted in the equations for the effective interaction and the self-energy, until finally convergence for all poles and residues is obtained. One should note that this approximation goes beyond the quasiparticle approach, where one demands only convergence of the quasiparticle spectrum.

Several discretization schemes can be devised that generate the specific locations and corresponding residues of the poles. Of course, such a scheme must lead to an approximated spectral function that retains the most important physical properties of the exact spectral function (e.g., the location and strength of the quasiparticle peak).

Motivated by its success in the description of the long-range correlations in finite nuclei [31–34], we used the BAsis GEnerated by Lanczos-scheme (BAGEL) scheme as a first attempt for a discrete representation of the spectral function [35,36]. However, when applied to the nuclear matter problem the results of the BAGEL scheme turned out to be unsatisfactory. Within the BAGEL schemes the discrete poles and strengths are chosen in such a way that the lowest-order energy-weighted moments of the complete spectral function

$$m_k(p)=\sum_i f_i(p)[F_i(p)]^k+\sum_j b_j(p)[B_j(p)]^k = \int_{-\infty}^{+\infty}\omega^k S(p,\omega)d\omega \quad \forall\ p \tag{12}$$

are reproduced. Due to the short-range correlations the background contribution to the spectral function is very asymmetric and the moments (12) are strongly dominated by the tail at high positive energies. As a result the central pole of the BAGEL spectrum not only represents the quasiparticle part of the spectral function, but also contains a considerably contribution from the background at high positive energies. For a three-pole calculation and using a reduced version of the interaction, this results in a central pole, located about 20 MeV above the on-shell energy. This pole carries 99% of the total strength, even though the quasiparticle strength at the Fermi momentum only amounts to 80% [35]. As a consequence, the induced depletion is much too small to remove the pairing instabilities, and a calculation with the full interaction near equilibrium density remains impossible. An attempt to improve the three-pole BAGEL scheme by using a larger number of poles revealed that one cannot get satisfying results with a limited number (up to 15) of poles. A feedback mechanism shifts the additional poles to very high energies and reattributes their strength to the central pole.

It is clear that this shortcoming of the BAGEL scheme can be remedied by constructing discretization schemes that allow for a closer correspondence between the quasiparticle excitation and one of the discrete poles. In the following we discuss three-pole approximations to the Green's function where we put the central pole at the quasiparticle on-shell energy and assign a certain quasiparticle strength to it. Furthermore, we demand reproduction of the zeroth- and first-order energy-weighted moment of the spectral function, separately in the particle and hole domain, i.e., for $k=0$ and $k=1$,

$$m_k^<(p)=\sum_j b_j(p)[B_j(p)]^k=\int_{-\infty}^{\epsilon_F}\omega^k S_h(p,\omega)d\omega \quad \forall\ p,$$

$$m_k^>(p)=\sum_i f_i(p)[F_i(p)]^k=\int_{\epsilon_F}^{+\infty}\omega^k S_p(p,\omega)d\omega \quad \forall\ p, \tag{13}$$

thereby fixing the location and strength of both other poles.

The remaining difficulty is to determine how much strength is attributed to the central pole. This strength should be a good measure of the quasiparticle strength, but except for momenta close to k_F, the separation of the quasiparticle peak from the background distribution is somewhat ambiguous.

The conventional expression for the quasiparticle strength

$$z_{\rm qp}(p)=\left(1-\left.\frac{\partial\,{\rm Re}\,\Sigma(\omega,p)}{\partial\omega}\right|_{\omega=\epsilon_{\rm qp}(p)}\right)^{-1}, \tag{14}$$

derived by expanding the spectral function around the quasiparticle energy, may not give reasonable results for all momenta. This fact was also observed by de Jong and Lenske [30] and is one of the problems encountered in an extended quasiparticle calculation [37].

For this reason we looked at other ways of separating the quasiparticle peak from the background. There are several possibilities of doing this. In order to test the sensitivity to the specific discretization scheme, we will present results for two quite distinct three-pole discretization schemes, labeled A and B. Scheme A starts from a very basic assumption on the distribution of the strength, whereas scheme B is more elaborate and yields a more realistic momentum dependence of the quasiparticle strength, similar to that found in other calculations [20,38,39]. As it turns out, schemes A and B produce surprisingly similar results for the binding energy.

In both schemes A and B, the hole spectral function for hole states ($p<k_F$) is represented by two poles labeled E_- and E_c (with corresponding residues R_- and R_c), which reproduce the two lowest-order moments of the hole spectral function,

$$R_-(p)+R_c(p)=m_0^<(p),$$

$$R_-(p)E_-(p)+R_c(p)E_c(p)=m_1^<(p). \tag{15}$$

The energy of the central pole is fixed at the on-shell energy

$$E_c(p)=\epsilon_{\rm qp}(p). \tag{16}$$

The particle spectral function for hole states is approximated by a single pole E_+ with strength R_+, simply determined by demanding that the two lowest-order moments of the particle spectral function are reproduced,

$$R_+(p)=m_0^>(p),$$

$$E_+(p)=m_1^>(p)/m_0^>(p). \tag{17}$$

For particle states ($p>k_F$) a corresponding approximation is used, where the hole spectral function is approximated by a single pole, and the particle spectral function by two poles.

In scheme A, a constant fraction of the integrated hole strength is attributed to the central pole for all hole states. This fraction is taken to be the same as the value at $p=k_F$,

$$R_c(p)=\frac{R_c(k_f)}{R_c(k_f)+R_-(k_f)}m_0^<(p),$$

$$R_-(p)=\frac{R_-(k_f)}{R_c(k_f)+R_-(k_f)}m_0^<(p), \tag{18}$$

$$p<k_F.$$

For particle states we have likewise

$$R_c(p)=\frac{R_c(k_f)}{R_c(k_f)+R_+(k_f)}m_0^>(p),$$

$$R_+(p)=\frac{R_+(k_f)}{R_c(k_f)+R_+(k_f)}m_0^>(p), \tag{19}$$

$$p>k_F.$$

It should be noted that $R_-(k_F)$, $R_c(k_F)$, and $R_+(k_F)$ are unambiguously defined, since the quasiparticle pole for the Fermi momentum lies at the Fermi energy, has zero width, and is completely isolated from the background distribution. $R_-(k_F)$ and $R_+(k_F)$ can be obtained by integrating the smooth hole and particle spectral function, while $R_c(k_F)$ corresponds to the missing strength in the sum rule,

$$R_c(k_F)=1-R_-(k_F)-R_+(k_F). \tag{20}$$

The assumption that the ratio of quasiparticle strength R_c over total occupation or depletion is independent of momentum is an oversimplification, especially in the limit of very large momenta where we expect R_c to approach unity. On the other hand, for such large momenta, the energy difference between both forward poles becomes small, and they can be regarded as a single degenerate pole.

In scheme B we try explicitly to extract a measure of the strength contained in the quasiparticle peak. This problem is not, as mentioned before, free from ambiguities, but the following scheme works very well in practice. For hole states, we assume that the hole spectral function can be written as the sum of a quasiparticle and a background model distribution,

$$S_h(p,\omega)=\frac{R_c(p)}{W_c(p)}f\left(\frac{\omega-E_c(p)}{W_c(p)}\right)+\frac{R_-(p)}{W_-}f\left(\frac{\omega-E_-(p)}{W_-}\right). \tag{21}$$

The normalized model distribution f is taken as

$$f(x)=\frac{1}{2+\pi}\left(\theta(|x|-1)e^{1-|x|}+\theta(1-|x|)\frac{2}{1+x^2}\right), \tag{22}$$

i.e., a Lorentzian form in the central region and exponential tails. The width W_c of the quasiparticle peak is taken equal to

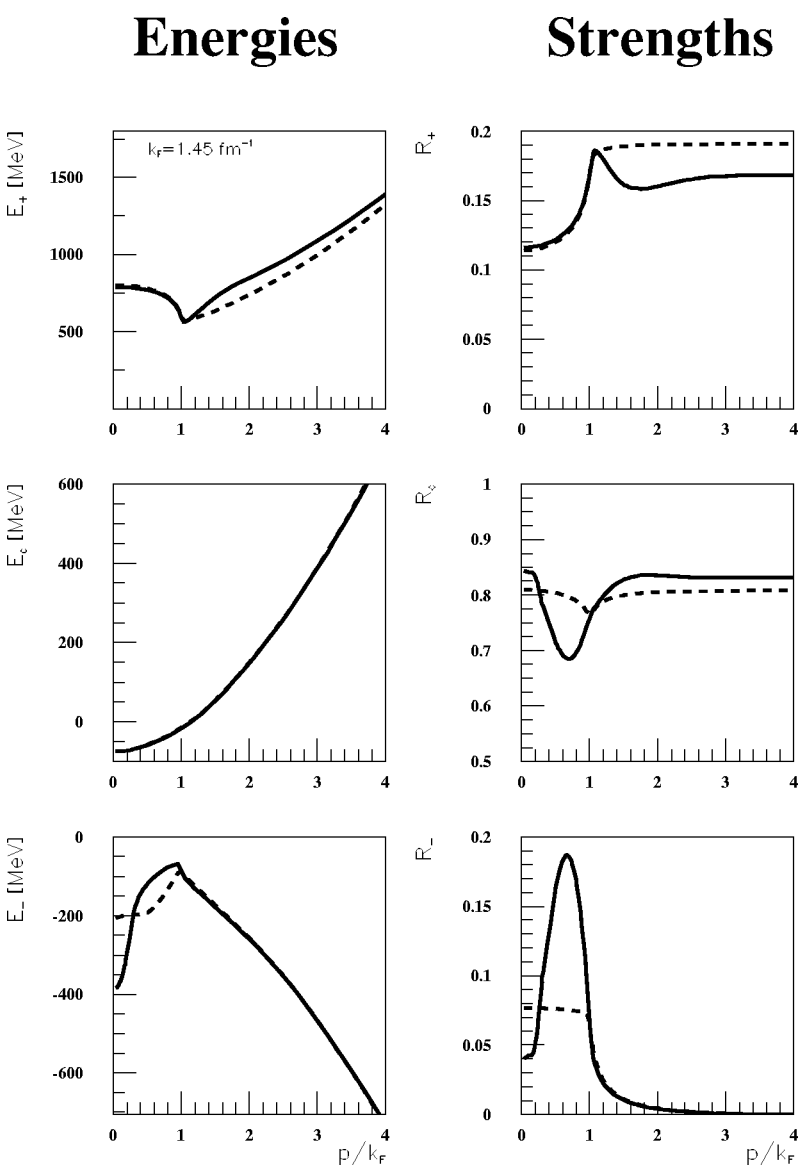

FIG. 3. Energies and single-particle strengths obtained in the discretization schemes A (dashed line) and B (full line), after convergence. The density corresponds to a Fermi momentum $k_F = 1.45$ fm^{-1}, and the Reid 93 interaction has been used.

$$W_c(p) = \frac{2\pi}{(2+\pi)} R_c(p) |\mathrm{Im}\,\Sigma(p, E_c(p))|, \tag{23}$$

where the factor $2\pi/(2+\pi) \sim 1.22$ corrects the peak value $(R_c/W_c) f(0)$ to the peak value $1/|\pi\,\mathrm{Im}\,\Sigma(p, \epsilon_{\mathrm{qp}}(p))|$ of the standard Lorentzian local approximation to the quasiparticle peak. The width W_- of the background distribution is assumed to be independent of single particle momentum p, and is estimated on the basis of the background distribution for $p = k_F$, which is unambiguously defined. The energy E_c of the central pole follows from Eq. (16), so we need three more conditions to determine R_c, E_-, and R_-. Two conditions are given by Eq. (15). As the third condition we demand that the true spectral function and the model distribution in Eq. (21) yield the same value for the integrated strength β in an interval around E_c,

$$\beta = \int_{E_c-\Delta}^{E_c+\Delta} d\omega\, S_h(p, \omega), \tag{24}$$

where $\Delta(p) = \sqrt{\sigma(p) |\mathrm{Im}\,\Sigma(p, E_c(p))|}$. This choice of Δ (in which σ is the standard deviation of the hole strength distribution) is heuristic, but it ensures that $\Delta(p) \to 0$ as $p \to k_F$, so that in this limit the sampled interval exclusively filters out the quasiparticle peak. The treatment of the particle states $(p > k_F)$ is completely analogous to that of the hole states.

Figure 3 displays the momentum dependence of the discrete poles and residues in scheme A and B, for a calculation with the Reid 93 interaction, after convergence has been obtained. Starting from a free spectrum, typically about 7 iterations are needed to obtain sufficiently converged spectra.

In both schemes the same value is obtained for the energy of the central pole E_c. This is not a trivial statement, as it indicates that after convergence both schemes yield the same position for the quasiparticle peak. The strength of the central pole R_c is the most significant difference of both calculations. Scheme A shows a strength that is proportional to $n(p)$ for $p < k_F$ and to $d(p) = 1 - n(p)$ for $p > k_F$, whereas scheme B has a more realistic momentum dependence. This includes a minimum located just below the Fermi momentum, balanced by a maximum in R_-.

The energy E_+ of the forward background pole is comparable in both schemes and is determined by the repulsive core of the interaction. Older interactions with stronger repulsion, such as the original version of the Reid interaction [40], will lead to a much higher value of E_+.

The energy E_- of the backward background pole is different in both schemes for momenta $p<k_F$, but shows the same behavior, $E_-\sim -p^2/2m$, for momenta $p>k_F$. This is the pole responsible for the high-momentum components in the nuclear many-body wave function.

For large momenta R_- quickly drops to zero. The forward background is much more persistent, because of the slow fall-off of $\mathrm{Im}\,\Sigma$ at large ω. In the $p\to\infty$ limit, scheme B eventually concentrates all strength in the central pole located at the free energy, i.e., $R_c\to 1$ and $R_+\to 0$, as one would expect on intuitive grounds. This regime, however, is only reached for very large momenta, not shown on the plot. In scheme A both R_c and R_+ have nonvanishing strengths in this limit, but as the corresponding energies have about the same value, they can also be interpreted as a single pole.

IV. EFFECTIVE INTERACTION

The discrete-pole approximation to the Green's function can be regarded as an extension of the quasiparticle approach, where the single pole is replaced by a set of multiple isolated poles. Consequently, the effective interaction can be evaluated using a procedure similar to the one developed in Ref. [27]. First of all it will be useful to perform a partial wave decomposition of the potential. Inserting the spectral functions corresponding to the discrete Green's function of Eq. (11),

$$S_p(p,\omega)=\sum_i f_i(p)\,\delta(\omega-F_i(p)),$$

$$S_h(p,\omega)=\sum_i b_i(p)\,\delta(\omega-B_i(p)) \tag{25}$$

into Eq. (5), the ladder equation in partial wave decomposition reads

$$\langle q|\Gamma^{JST}_{LL'}(P,\Omega)|q'\rangle=\langle q|V^{JST}_{LL'}|q'\rangle+\sum_{i_1 i_2 L''}\int_0^\infty dq''q''^2\langle q|V^{JST}_{LL''}|q''\rangle\frac{\overline{f_{i_1}(p_1)f_{i_2}(p_2)}}{\Omega-\overline{[F_{i_1}(p_1)+F_{i_2}(p_2)]}+i\eta}\langle q''|\Gamma^{JST}_{L''L'}(P,\Omega)|q'\rangle$$

$$-\sum_{j_1 j_2 L''}\int_0^\infty dq''q''^2\langle q|V^{JST}_{LL''}|q''\rangle\frac{\overline{b_{j_1}(p_1)b_{j_2}(p_2)}}{\Omega-\overline{[B_{j_1}(p_1)+B_{j_2}(p_2)]}-i\eta}\langle q''|\Gamma^{JST}_{L''L'}(P,\Omega)|q'\rangle, \tag{26}$$

where $\vec{p}_{1,2}=\vec{P}/2\pm\vec{q}''$. In this equation the bar over strength functions and energies denotes that the dependence on the angle between $\vec{q}''$ and $\vec{P}$ has been averaged out (see the Appendix).

Angle averaging of the two-particle propagator is necessary to decouple the different partial waves, thereby reducing the dimension of the matrix that needs to be inverted in order to obtain Γ. In our calculations the numerator and denominator are averaged independently of each other. The validity of this approach was first discussed in Refs. [41,42]. In Ref. [43] the effects of several angle-averaging procedures are checked in the case of a Brueckner-Hartree-Fock calculation with a Reid soft-core interaction. A full calculation without any angle averaging is compared with a calculation in which all angular dependency of the two-particle propagator is eliminated and a calculation in which only the denominator is angle-averaged. It turns out that the discrepancies in binding energy and the complex optical potential are quite small for the different approximations at saturation density. This is confirmed by recent studies [44,45], although a systematic increase in binding is found for increasing density, which is larger in the continuous choice BHF calculation.

Equation (26) is solved using the two-step procedure of Ref. [46]. First a real reaction matrix R is calculated by including only the principal value part of the complex integrals. A regularized version of this integral equation on a grid in relative momentum space is solved by matrix inversion. In a second step the real and imaginary parts of the Γ matrix are calculated from the reaction matrix. The standard procedure has to be extended to handle the presence of more than one singularity in case of a multiple-pole approximation. This is explained in more detail in the Appendix.

Since we first want to investigate how the incorporation of off-shell effects modifies the Γ matrix as compared to a quasiparticle (single-pole) calculation, we use in this section a reduced version of the Reid 93 interaction, where the $^1S_0$ and the $^3S_1$-$^3D_1$ partial waves are multiplied by a factor 0.75 and 0.5, respectively. This is done solely to avoid the appearance of pairing instabilities in the quasiparticle calculation and to make the comparison possible. In the final multiple-pole calculations of the next sections, the full Reid 93 potential is used.

Partial waves up to $J=3$ are included in the effective interaction, as contributions of higher-order partial waves are negligible [36,47]. Higher partial waves are incorporated in the Hartree-Fock part of the self-energy, where it was found necessary to include partial waves up to $J=9$ [36].

The energy dependence of the imaginary part of Γ is closely linked to the poles of the two-particle propagator. In

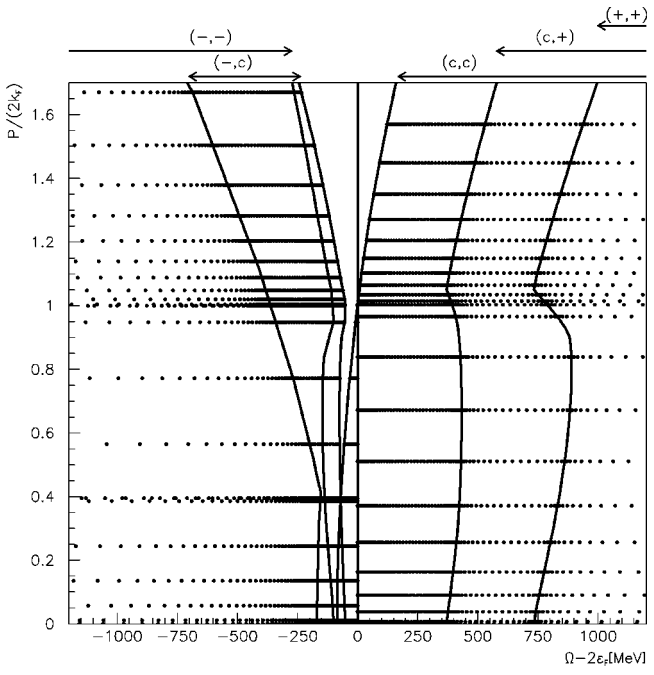

FIG. 4. The choice of the (Ω,P)-interpolation points in the map for the effective interaction Γ. The solid lines correspond to the boundaries of different two-particle channels, as explained in the text.

the quasiparticle calculation $\mathrm{Im}\,\Gamma$ will only be nonvanishing for energies above a threshold energy,

$$\Omega_{\mathrm{min}}^{\mathrm{qp}}=2\epsilon_{\mathrm{qp}}(P/2), \tag{27}$$

which is the minimum energy of two particles with a center-of-mass momentum P. This picture gets more complicated within the multiple-pole scheme of Eq. (26), as singularities can now appear within different two-particle channels (i_1,i_2) and (j_1,j_2).

This results in a much more complex pattern of zones of nonvanishing $\mathrm{Im}\,\Gamma$ in the (Ω,P) plane. This structure is illustrated in Fig. 4 for scheme A; the same features are present for scheme B. The full lines correspond to the threshold energies as a function of P for each of the possible two-particle channels. The (c,c) channel exhibits a minimum energy similar to the quasiparticle case. This means that for all energies above this threshold value a singularity will be found in the (c,c) channel. The $(-,c)$ exhibits both a minimum and maximum energy, so that only in this finite energy range this specific channel will contribute to $\mathrm{Im}\,\Gamma$. The $(-,-)$ channel has a maximum energy, and its singularities will be found for all energies below this threshold value. Both the $(c,+)$ and $(+,+)$ channels extend from a minimum energy up to $+\infty$. Specific details on the origin of these threshold values can be found in Ref. [36]. It should also be noted that, since the $(-,c)$ and $(c,+)$ two-particle energies are not necessarily monotonic functions of the relative momentum, more than one singularity can be found for a fixed (Ω,P) value.

The matrix inversion used for solving the ladder equation makes the evaluation of the effective interaction the most time-consuming step of the iterative scheme. Therefore it is useful to construct at the start of each iteration, a map of the imaginary part of the effective interaction on a grid of (P,Ω,q) points. When specific values of $\mathrm{Im}\,\Gamma(P,\Omega,q)$ are needed in the evaluation of the self-energy, they can be obtained from a threefold interpolation of the values in this map. The Ω and P grids are illustrated by the dots in Fig. 4. For an accurate calculation 100 mesh points are needed for the Ω grid, while 31 mesh points proved to be sufficient for the P grid. Due to the complicated structure of the different, often overlapping zones of nonvanishing $\mathrm{Im}\,\Gamma$ in the (Ω,P) plane, a careful construction of these grids is crucial for the convergence of the iterative procedure. Again we refer to Ref. [36] for additional details.

The effective interaction calculated with a three-pole Green's function using discretization scheme A is presented in Fig. 5 for two center-off-mass momenta: one below and one above the critical value $2k_F$. For this critical value the (c,c) channel will no longer contain a singularity for energies below $2\epsilon_F$. Backward $(\Omega<2\epsilon_F)$ and forward $(\Omega>2\epsilon_F)$ parts are shown in separate graphs because of the large difference in the relevant energy range. These results are compared with the effective interaction calculated within a quasiparticle calculation (dashed line). The energy scale is relative to $2\epsilon_F$ to allow an easy comparison of both results.

The most pronounced differences are found for $\Omega<2\epsilon_F$, where the presence of the additional $(-)$ pole in the Green's function leads to the appearance of strength below the hh threshold energy of the quasiparticle calculation. In the $P=k_F$ plot the (c,c) contribution still dominates the three-pole calculation of $\mathrm{Im}\,\Gamma$. However, it is reduced in strength compared to the quasiparticle calculations, in conformity with the reduced strength of the central pole. At the same time, an extra contribution, absent in the quasiparticle approach, can be observed at energies below -74 MeV. This contribution originates from the $(-,c)$ channel. At energies below -144 MeV also the $(-,-)$ channel starts contributing, but due to the relatively small strength of the $(-)$ pole, these contributions are less important, although they extend to very large negative energies. It should be noted that the contribution to $\mathrm{Im}\,\Gamma$ of a specific two-particle channel is proportional to the value of the angle-averaged projection operator for this channel, evaluated in the corresponding singularity. This quantity scales as the product of both strength functions, which explains the relative size of the contributions originating from different two-particle channels.

For $P=2.2k_F$ the imaginary part vanishes for all energies $\Omega<2\epsilon_F$ in the quasiparticle approach. This is no longer so for a three-pole calculation where both the $(-,-)$ and $(-,c)$ channel will contribute. The contribution of the $(-,-)$ channel is again much smaller than the one of $(-,c)$, but is nevertheless visible as the peak around -125 MeV.

The redistribution of the quasiparticle strength also leads to differences in $\mathrm{Im}\,\Gamma$ for $\Omega>2\epsilon_F$. For both $P=k_F$ and $P=2.2k_F$, there is a shift towards higher energies, caused by the strength of the $(+)$ pole. For $P=k_F$ the opening of the $(c,+)$ channel leads to a sharp peak around 430 MeV. In a

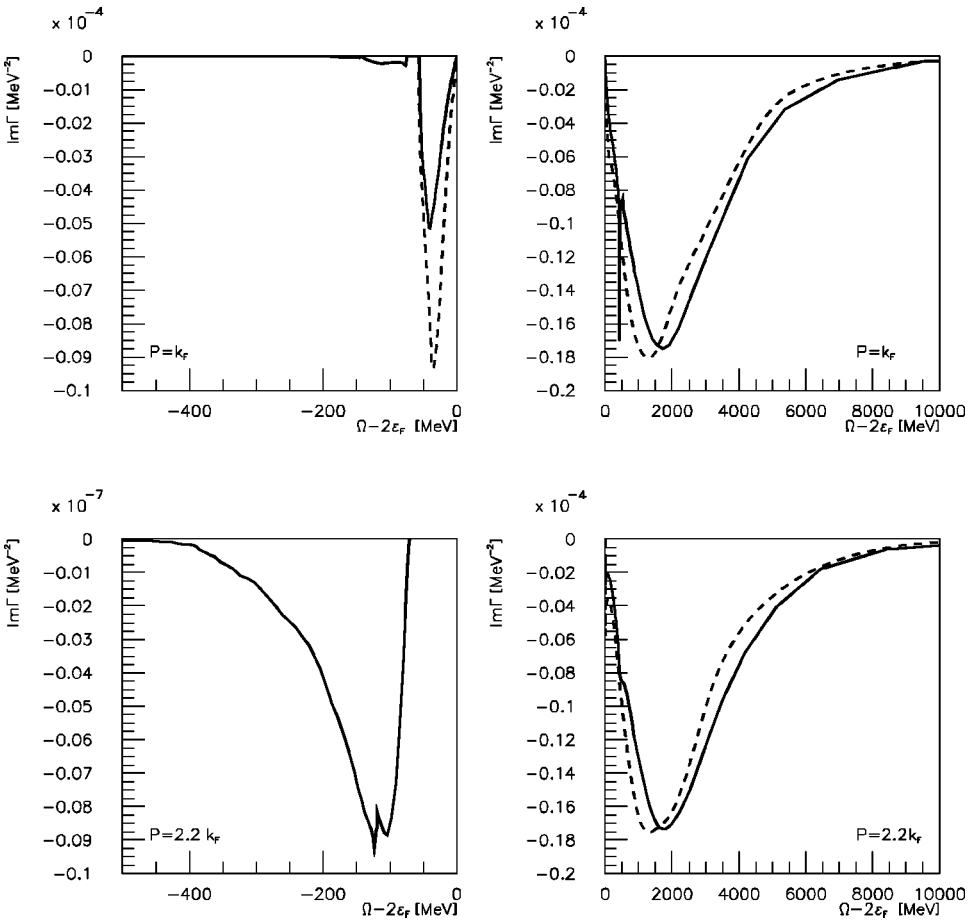

FIG. 5. The Ω dependence of $\mathrm{Im}\,\Gamma(P,\Omega,q)$, the imaginary part of the effective interaction summed over all partial waves $J \leqslant 3$. Results are obtained for the reduced Reid 93 potential and $k_F = 1.45$ fm^{-1}. Upper panel: $q=0$ and $P=k_F$. Lower panel: $q=0$ and $P=2.2k_F$. The dashed line corresponds to the quasiparticle approach, the full line to the three-pole discretization scheme A.

narrow range above this energy the $(c,+)$ channel contains a double singularity, causing an enhanced contribution to $\mathrm{Im}\,\Gamma$. For slightly higher energies, the second singularity disappears, explaining the peaked structure. There is no double singularity in this channel for $P=2.2k_F$, leading to a smoother energy dependence of $\mathrm{Im}\,\Gamma$. To conclude this section, it should be stressed that these shell-like structures of $\mathrm{Im}\,\Gamma$ result from the discrete-pole approach. If one retains the full energy dependence of the spectral function in the evaluation of effective interaction, these structures are smoothed out [19,20,48].

V. PAIRING CORRELATIONS

As was mentioned before, the incorporation of intermediate hh propagation may lead to complex poles in the effective interaction [18]. Therefore a reduction of the Reid 93 interaction was needed in order to obtain the quasiparticle results shown in the preceding section. The imaginary part of the effective interaction calculated within a quasiparticle scheme and using the complete Reid 93 interaction is shown in Fig. 6. Around $2\epsilon_F$ the imaginary part Γ is completely dominated by a singularity, originating from two complex conjugate poles in the effective interaction. This singularity leads to an unphysical self-energy and spectral functions, reflecting the phase transition to a superfluid ground state. A calculation within the framework outlined above will be highly unstable [49,50]. One can overcome these difficulties

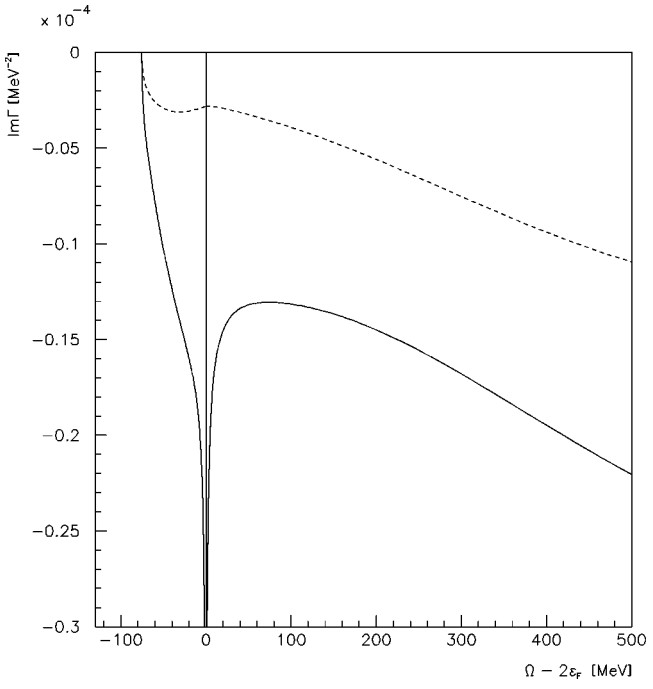

FIG. 6. The Ω dependence of the imaginary part of the effective interaction within the quasiparticle approximation, for $P=0$ and $q=0$ ($k_F=1.45$ fm^{-1}). The full line corresponds to the complete Reid 93 interaction, and the dashed line to the reduced version (see text), where no pairing instabilities are present.

either by using a reduced interaction [27] or by introducing a gap in the single-particle spectrum [29]. A complete treatment of the paired phase should include anomalous propagators and self-energy [51,52].

This discussion does not imply that nuclear matter near equilibrium density is *a priori* superfluid. Pairing correlations are very sensitive to the occupation of single-particle states close to the Fermi surface. Both thermal effects and correlations tend to smear out the Fermi surface and decrease the effects of pairing [17,53].

The ladder approximation for the effective interaction regulates the effects of short-range correlations, originating from the repulsive core of the *NN* potential, but at the same time it also introduces collective effects from the attractive components of the interaction. In order to see how summing ladder diagrams leads to paired nucleon solutions, we transform the Bethe-Goldstone equation into a two-body Schrödinger equation. Since the largest pairing instability is found for zero center-of-mass momentum [16,27,36], we restrict ourselves to solving the ladder equation for $P=0$,

$$\Gamma(\Omega)=V+Vg_{\mathrm{II}}^{(0)}(\Omega)\Gamma(\Omega). \tag{28}$$

Here V, Γ, and $g_{\mathrm{II}}^{(0)}$ are regarded as matrices indexed by relative momentum. In this equation $g_{\mathrm{II}}^{(0)}$ stands for the free two-body propagator,

$$g_{\mathrm{II}}^{(0)}(\Omega,q,q')=\delta(q-q')\left[\frac{\theta(q-k_F)}{\Omega-q^2/m+i\eta}-\frac{\theta(k_F-q)}{\Omega-q^2/m-i\eta}\right]. \tag{29}$$

The effective interaction Γ also defines a correlated two-particle propagator g_{II},

$$\Gamma(\Omega)=V+Vg_{\mathrm{II}}(\Omega)V, \tag{30}$$

which is related to the uncorrelated propagator as

$$g_{\mathrm{II}}^{(0)}(\Omega)V=g_{\mathrm{II}}(\Omega)\Gamma(\Omega). \tag{31}$$

This expression indicates that the singularities of the effective interaction are also singularities of the correlated two-particle propagator. The ladder equation implies the following relation between correlated and uncorrelated two-particle propagators:

$$g_{\mathrm{II}}(\Omega)=\frac{g_{\mathrm{II}}^{(0)}(\Omega)}{1-g_{\mathrm{II}}^{(0)}(\Omega)V}=\frac{1}{g_{\mathrm{II}}^{(0)}(\Omega)^{-1}-V}. \tag{32}$$

Finding the singularities of the Γ matrix is equivalent to finding the zero eigenvalues of the following matrix:

$$g_{\mathrm{II}}^{(0)}(\Omega)^{-1}-V. \tag{33}$$

Using the free two-particle propagator of Eq. (29), and distinguishing between the hole and the particle components of the eigenvector, this eigenvalue equation for a specific partial wave can be written as

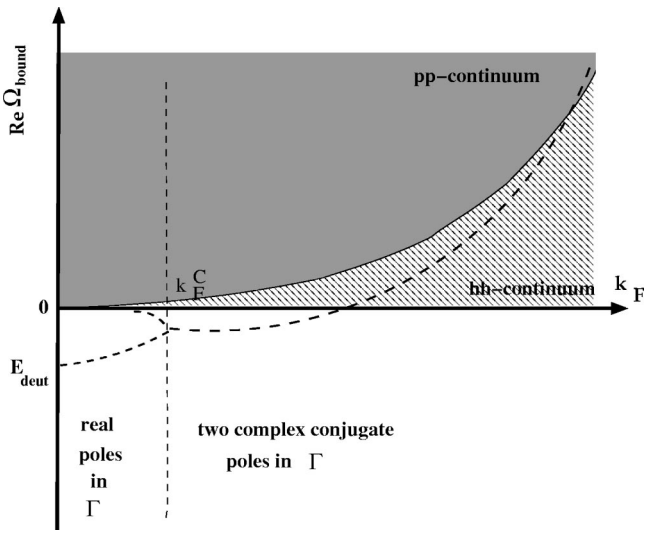

FIG. 7. An illustration of the location of the poles of the effective interaction in the ${}^3S_1$-${}^3D_1$ channel. A free spectrum has been used. The continuum (above zero) has been divided into pp and hh regions. The position of the isolated poles is given by the dashed lines. Below the critical density k_F^C one or two isolated real poles are found. At zero density the isolated real pole is located at the deuteron energy E_{deut}. At densities above the critical density the real part of the complex conjugate poles in Γ is plotted.

$$\left[T+\begin{pmatrix}-I & 0\\ 0 & I\end{pmatrix}V^{JST}\right]\begin{pmatrix}\psi^{(h)}\\ \psi^{(p)}\end{pmatrix}=\Omega\begin{pmatrix}\psi^{(h)}\\ \psi^{(p)}\end{pmatrix}, \tag{34}$$

where I is the identity matrix. In this equation the kinetic energy T is a diagonal matrix in the relative momentum space, having q^2/m on the diagonal. In coupled channels the dimensions of the matrices are doubled.

The matrix on the left-hand side of Eq. (34) is not symmetrical, allowing both real eigenvalues and pairs of complex conjugate eigenvalues, depending on the density and the specific partial wave. The following characteristic energy spectrum is obtained:

(1) A continuum of real poles in the interval $[0,2\epsilon_F]$, corresponding to unbound hh excitations.

(2) A continuum of real poles in the interval $[2\epsilon_F,\infty]$, corresponding to unbound pp excitations.

(3) In a certain density range, an isolated real pole located below the hh continuum. This pole corresponds to a bound state with $\Omega_{\mathrm{bound}}<0$.

(4) In a certain density range, two complex conjugate poles can appear at energies $\Omega_{\mathrm{bound}}=\Omega_R\pm i\Omega_I$, corresponding to bound states with energies located within or very close to the continuum.

The location of these poles as function of the density is presented schematically in Fig. 7. The appearance of complex poles is a result of the inclusion of hh propagation as noted by Dickhoff [18]. Within a BHF scheme, thus neglecting hh propagation in the two-particle propagator, the corresponding eigenvalue equation looks as

$$\left[T+\begin{pmatrix}0 & 0\\ 0 & I\end{pmatrix}V^{JST}\right]\begin{pmatrix}\psi^{(h)}\\ \psi^{(p)}\end{pmatrix}=\Omega\begin{pmatrix}\psi^{(h)}\\ \psi^{(p)}\end{pmatrix}. \tag{35}$$

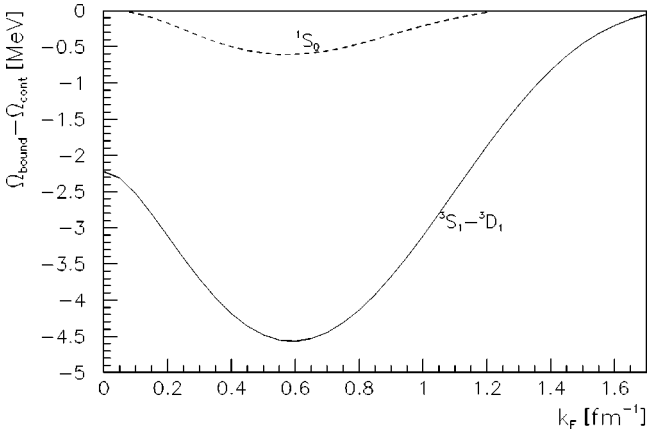

FIG. 8. The energy of the bound state in a Brueckner calculation at $P=0$, with a free single-particle spectrum and using the Reid 93 interaction. Energies are relative to the threshold energy for the pp continuum ($\Omega_{\min}^{\text{cont}}=2\epsilon_F$). The full line corresponds to the $^3S_1$-$^3D_1$ deuteron channel, the dashed line to the $^1S_0$ channel.

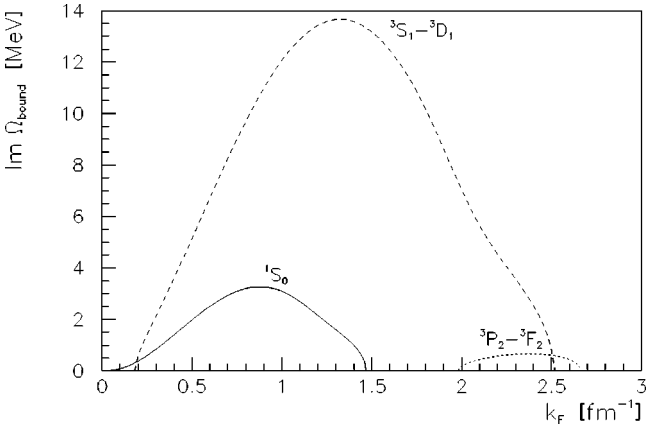

FIG. 9. The imaginary part of the complex pole in the effective interaction in a quasiparticle calculation for $P=0$, with a free single-particle spectrum and using the Reid 93 interaction. Results are plotted for three different partial waves as a function of the density.

Since the matrix on the right-hand side of Eq. (35) is now symmetrical, all eigenvalues will be real. Still, a single bound state can be found at energies below the pp continuum (Fig. 8). These bounds states appear both in the $^1S_0$ and the $^3S_1$-$^3D_1$ partial waves. In the absence of the medium ($k_F\rightarrow 0$) only the $^3S_1$-$^3D_1$ bound state remains. This state can be identified as the deuteron solution of the two-particle Schrödinger equation. In most Brueckner-type calculations these bound state are omitted, since their effect on properties such as binding energy and occupation probability is very small, as was argued in Ref. [29]. At higher densities these isolated poles in the Γ matrix will eventually disappear.

When hh propagation is incorporated in the effective interaction, bound states may manifest themselves as a pair of complex poles in a certain density range. In this particular case the bound states will cause sharp spikes in the effective interaction (Fig. 6), and can no longer be neglected as they hinder a numerically stable calculation. The many-body scheme as outlined in this paper must then be adjusted to account for these bound states explicitly [51].

Figure 9 shows the imaginary part of the resulting complex poles as a function of the density for a number of partial waves. Two partial waves, $^3S_1$-$^3D_1$ and $^1S_0$, lead to an instability at the empirical saturation density. The deuteron channel causes the largest instability, which is in conformity with the observations made in Refs. [27,47]. A third instability shows up at higher densities. This instability originates from the $^3P_2$-$^3F_2$ channel and is missing in a Brueckner calculation. Hence this pairing at higher densities is a pure result of the incorporation of intermediate hh propagation. Comparing Fig. 8 with Fig. 9, one should note that also for the $^3S_1$-$^3D_1$ and $^1S_0$ multipoles, hh propagation will seriously enhance the density range in which bound states are formed.

Up to now we used pp and hh projection operators, defined with respect to the uncorrelated Fermi sea. Short-range correlations will deform this Fermi sea. The correlated pairing propagators may remove the pairing instability in a density range around the empirical saturation density, since pairing correlations are very sensitive to the number of states available near the Fermi surface. Short-range correlations yield a depletion of the hole states, and a partial occupation of the particle states just above the Fermi surface. This reduces the effective interaction near the Fermi surface, thereby diminishing the effects of the pairing correlations. If the reduction is large enough, the ground state of the system will not be superfluid.

The influence of short-range correlations on the pairing properties are thus similar to the well-known thermal effects. At finite temperatures ($T\neq 0$) thermal excitations also cause a deformation of the Fermi sea. Even in the absence of NN correlations, thermal effects lead to an occupation probability,

$$n(p)=\frac{1}{e^{(\epsilon(p)-\mu)/kT}+1}, \tag{36}$$

where k is Boltzmann's constant [16]. This distribution corresponds to the Fermi function of statistical physics. Above a

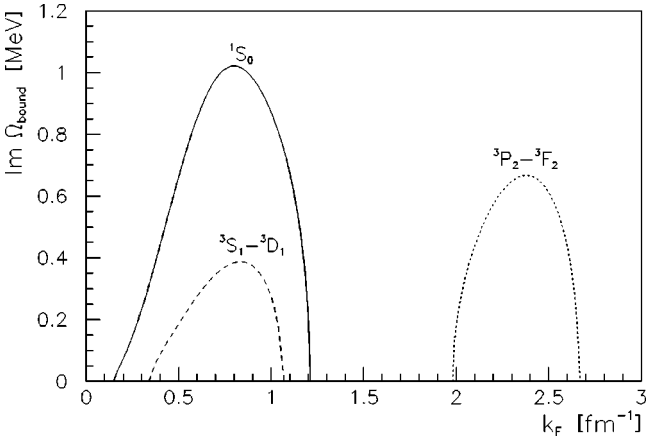

FIG. 10. Same as Fig. 9, but using the reduced Reid 93 interaction (see text).

critical temperature T_C this deformation will be large enough to lead to a normal ground state, while below T_C a superfluid ground state will be favored.

The deformation of the Fermi sea can be incorporated in the schematic model by modifying the projection operators in the eigenvalue equation (34),

$$\left[T+\begin{pmatrix} -n^2 & 0 \\ 0 & (1-n)^2 \end{pmatrix} V^{JST}\right]\begin{pmatrix} \psi^{(h)} \\ \psi^{(p)} \end{pmatrix} = \Omega \begin{pmatrix} \psi^{(h)} \\ \psi^{(p)} \end{pmatrix}, \quad (37)$$

for a specific partial wave. Using the Fermi function (36), a critical temperature of 0.7 MeV is obtained for the $^1S_0$ multipole, while a much higher temperature of 23 MeV is obtained for the more strongly attractive deuteron channel.

The effects of short-range correlations can be simulated in the same way. Using, e.g., in Eq. (37) the occupation probabilities obtained in a three-pole calculation rather than the statistical Fermi function leads to a nonsuperfluid ground state at the empirical saturation density.

For completeness, Fig. 10 shows the imaginary part of the complex pole obtained with the reduced Reid 93 interaction as used in the preceding section. One sees that this reduction is sufficient to remove the complex poles around the empirical saturation density.

VI. SELF-ENERGY

For the evaluation of the self-energy we retain the first-order diagram in the effective interaction (Fig. 1). Similar to the effective interaction, the imaginary part of the self-energy exhibits an energy dependence that is far more complicated than the one obtained in quasiparticle calculations.

Inserting the multiple-pole approximation to the Green's function in Eq. (38) for the self-energy, we find

$$\Sigma(p,\omega)=\frac{1}{8\pi^2}\int dp' p'^2 \int_{-1}^{1} d(\cos\theta) V(q) \sum_j b_j(p') - \frac{1}{4\pi}\sum_i \int_{-\infty}^{2\epsilon_F} d\Omega' \int dp' p'^2 \int_{-1}^{1} d(\cos\theta) \frac{\mathrm{Im}\,\Gamma(P,\Omega',q)}{\omega-\Omega'+F_i(p')-i\eta} f_i(p')$$
$$-\frac{1}{4\pi}\sum_j \int_{2\epsilon_F}^{\infty} d\Omega' \int dp' p'^2 \int_{-1}^{1} d(\cos\theta) \frac{\mathrm{Im}\,\Gamma(P,\Omega',q)}{\omega-\Omega'+B_j(p')+i\eta} b_j(p'), \quad (38)$$

with $P=\sqrt{p^2+p'^2+2pp'\cos\theta}$ and $q=\sqrt{p^2+p'^2-2pp'\cos\theta}/2$. A shorthand notation was used for the sum over the different partial waves of the diagonal matrix elements,

$$\mathrm{Im}\,\Gamma(P,\Omega,q)=\sum_{LJST}(2J+1)(2T+1)\mathrm{Im}\langle q|\Gamma^{JST}_{LL}(P,\Omega)|q\rangle,$$

$$V(q)=\sum_{LJST}(2J+1)(2T+1)\langle q|V^{JST}_{LL}|q\rangle. \quad (39)$$

As the matrix elements are antisymmetrized, only channels with odd values of $L+S+T$ contribute to this sum.

Further discussions on the self-energy are simplified by noting that $\mathrm{Im}\,\Gamma(P,\Omega=2\epsilon_F,q)=0$ and defining [27] $\mathrm{Im}\,\Gamma^{\uparrow}$ and $\mathrm{Im}\,\Gamma^{\downarrow}$ through

$$\mathrm{Im}\,\Gamma(P,\Omega,q)=\theta(2\epsilon_F-\Omega)\mathrm{Im}\,\Gamma^{\uparrow}(P,\Omega,q) + \theta(\Omega-2\epsilon_F)\mathrm{Im}\,\Gamma^{\downarrow}(P,\Omega,q). \quad (40)$$

Using these functions the imaginary part of the self-energy can be written as

$$\mathrm{Im}\,\Sigma(p,\omega)=$$
$$-\frac{1}{4}\sum_i \int dP P^2 \int_{-1}^{1} d(\cos\theta)\mathrm{Im}\,\Gamma^{\uparrow}(P,\omega+F_i(p'),q) f_i(p)$$
$$+\frac{1}{4}\sum_j \int dP P^2 \int_{-1}^{1} d(\cos\theta)\mathrm{Im}\,\Gamma^{\downarrow}(P,\omega+B_j(p'),q) b_j(p). \quad (41)$$

The resulting imaginary part of the self-energy is plotted for three momenta in Fig. 11. Note the different energy scale used for the addition and removal domains. The imaginary part extends to very high positive energies, due to the short-range correlations.

The observed structures in $\mathrm{Im}\,\Sigma$ can be explained on the same grounds as the structure of $\mathrm{Im}\,\Gamma$. Inspecting Fig. 4 one sees that for a fixed value of P, a specific two-particle channel (i_1,i_2) generates an allowed Ω interval $[\Omega^{i_1,i_2}_{\min},\Omega^{i_1,i_2}_{\max}]$ for $\mathrm{Im}\,\Gamma$. In order to find a nonvanishing $\mathrm{Im}\,\Sigma$ at a certain energy ω there must be a triplet (i_1,i_2,j) and an allowed p' value such that

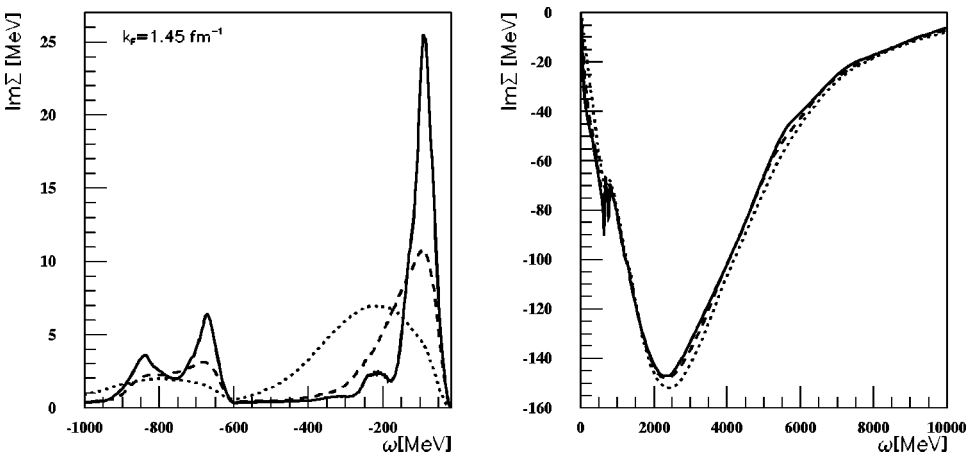

FIG. 11. The energy dependence of the imaginary part of the self-energy, in the three-pole scheme A, using the Reid 93 interaction at $k_F = 1.45$ fm^{-1}. The full line corresponds to $p=0$, the dashed line to $p=0.8k_F$, and the dotted line to $p=1.7k_F$.

$$\Omega_{\min}^{i_1,i_2}(P) < \omega + E_j(p') < \Omega_{\max}^{i_1,i_2}(P), \tag{42}$$

where $E_j(p')$ stands for $F_j(p')$ (if $\omega < \epsilon_F$) or $B_j(p')$ (if $\omega > \epsilon_F$). These requirements lead to a set of ω intervals that can be associated to different three-particle combinations $(i_1,i_2;j)$. The self-energy for $p=0$ is again shown in Fig. 12, where the contributions to the sum (41) originating from different poles f_i, b_j are displayed separately.

For $\omega < \epsilon_F$ the largest contributions originate from the (c) pole in the spectral function. For the large peak located near -100 MeV, this pole is coupled to the (c,c) part of the effective interaction Γ. This is the only contribution to the backward self-energy that remains in a quasiparticle calculation. The small shoulder at -250 MeV is the result of coupling the (c) part of the spectral function with the $(-,c)$ part of Γ. Between -800 MeV and -1000 MeV we find a considerable contribution originating from the $(+)$ pole of the single-particle propagator. The two peaks are again due to the coupling with the same (c,c) and $(c,-)$ parts of the effective interaction. The energy shift and relative magnitude of both contributions reflect roughly the difference in energy and strength of the (c) and $(+)$ poles.

At $\omega > \epsilon_F$ both the (c) and $(-)$ poles contribute over almost the complete energy range. The (c) contribution starts at the Fermi energy, the $(-)$ contribution at 60 MeV, in conformity with the energy difference of both poles. The shape of both contributions is similar, and the relative magnitude corresponds to the difference in strength of both poles. The peaked structure visible at 800 MeV reflects the peak visible in the imaginary part of the effective interaction at 450 MeV (Fig. 5). For the higher momenta in Fig. 11 the structures described above are more spread out.

The real part of the self-energy can be calculated from the dispersion relation and contains contributions from energies both above and below the Fermi energy,

$$\mathrm{Re}\,\Sigma(p,\omega) = \frac{1}{\pi}\mathrm{P}\int_{-\infty}^{\epsilon_F} d\omega' \frac{\mathrm{Im}\,\Sigma(p,\omega')}{\omega-\omega'} - \frac{1}{\pi}\mathrm{P}\int_{\epsilon_F}^{\infty} d\omega' \frac{\mathrm{Im}\,\Sigma(p,\omega')}{\omega-\omega'}. \tag{43}$$

The energy dependence of $\mathrm{Re}\,\Sigma$ and of both terms in Eq. (43) is displayed in Fig. 13, together with the corresponding $\mathrm{Re}\Sigma$ in a BHF calculation. Since the $\omega > \epsilon_F$ part of $\mathrm{Im}\,\Sigma$ is dominant, the overall energy dependence of $\mathrm{Re}\,\Sigma$ is similar to the BHF result. The detailed energy dependence can be traced back to the structure of $\mathrm{Im}\,\Sigma$, which was discussed previously.

The real part of the self-energy is used in the determination of the on-shell energy. In the energy range corresponding to the on-shell energies for the hole states there is a repulsive effect of the $\omega < \epsilon_F$ region in the dispersion inte-

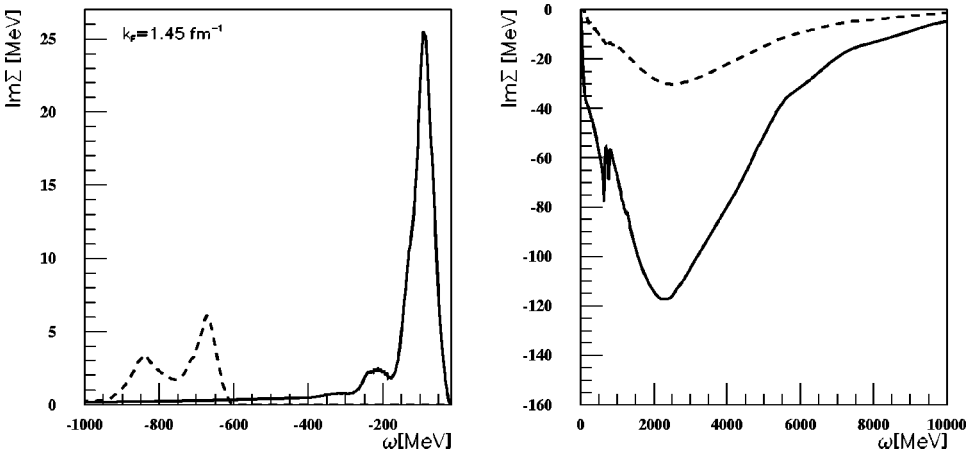

FIG. 12. The energy dependence of the different contributions to the imaginary part of the self-energy of Fig. 11 for $p=0$. Left panel: energy below ϵ_F. Right panel: energy above ϵ_F. The full line corresponds to the contribution of the (c) pole of the spectral function. The dashed line refers to the contribution of the $(+)$ pole in the left panel, and of the $(-)$ pole in the right panel.

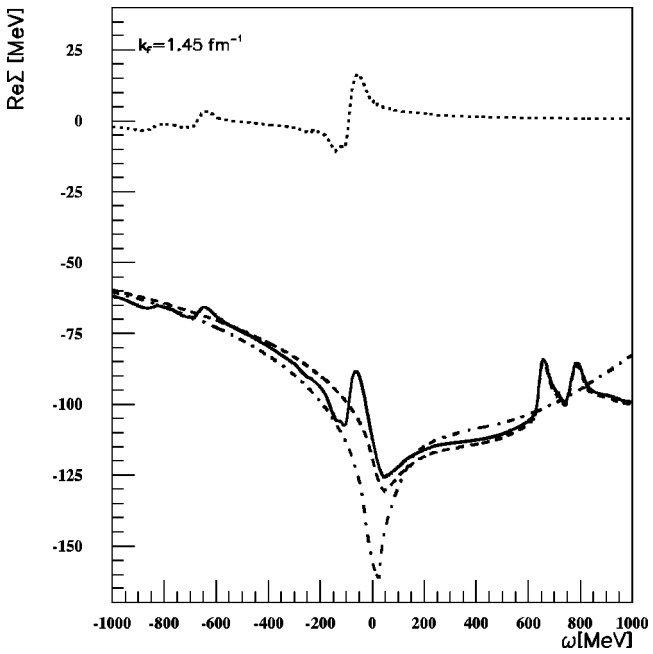

FIG. 13. The energy dependence of the real part of the self-energy, in the three-pole scheme A, using the Reid 93 interaction at $k_F = 1.45$ fm^{-1}. Contributions to the dispersion integral from energies below ϵ_F (dotted line) and energies above ϵ_F (dashed line) are plotted separately, as well as the total sum (full line). For comparison also the BHF result is shown (dash-dotted line).

gral. This is a result of the inclusion of hh propagation in the effective interaction, which is absent in BHF results.

VII. SPECTRAL FUNCTIONS AND BINDING ENERGY

Once the imaginary and real parts of the self-energy are determined, the spectral function is calculated using Eq. (4). Figure 14 compares the spectral functions obtained using three-pole scheme A with the ones obtained in a quasiparticle scheme, after convergence and for the reduced Reid 93 interaction. The most pronounced difference is found in the removal domain, where the hole spectral function in a quasiparticle calculation vanishes below a momentum-dependent miminum energy. Because of the redistribution of the single-particle strength, the spectral function extends to $-\infty$ within the self-consistent calculation. In both calculations the strength extends to large positive energies. Due to the quasiparticle reduction, a larger fraction of the strength appears at higher energies in the self-consistent calculation.

Note that the spectral function for $p=0$ displays a double peak in the quasiparticle calculation, signaling the breakdown of the quasiparticle description for small momenta. In the self-consistent calculation the spectral function exhibits a single peak, and the on-shell energy is unambiguously determined.

Figure 15 shows the hole and the particle spectral function for three different momenta, calculated using the full

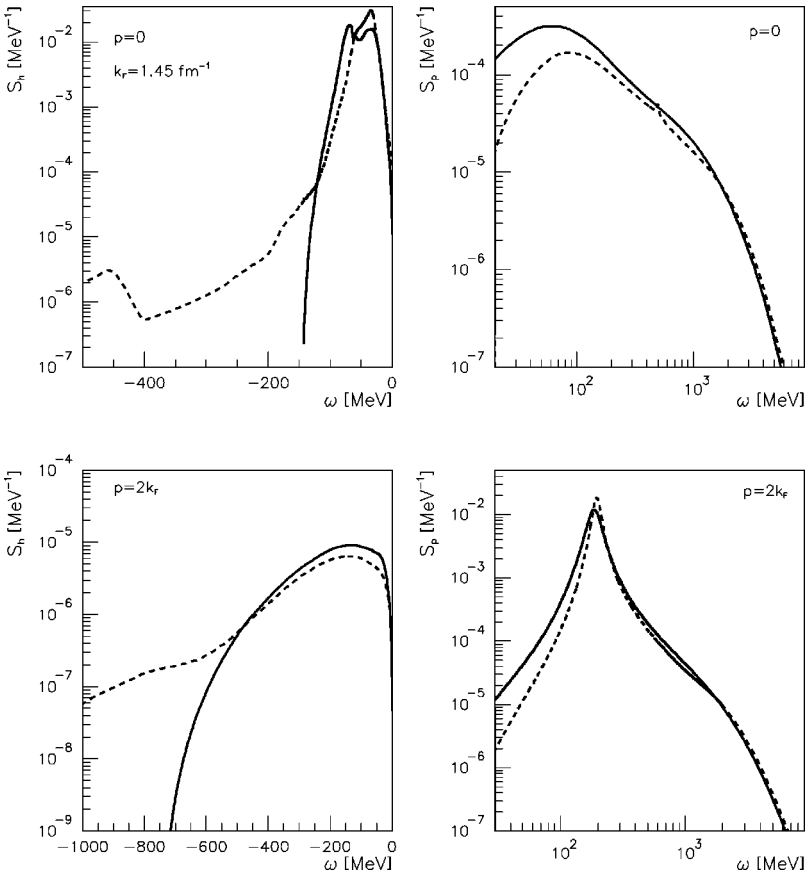

FIG. 14. The energy dependence of the spectral functions obtained using the reduced version of the Reid 93 interaction for $k_F = 1.45$ fm^{-1}. Left panels show the hole spectral functions, right panels the particle spectral functions, for $p=0$ (upper panels) and $p=2k_F$ (lower panels). The full line is the result of the quasiparticle approximation, the dashed line is the result obtained using the three-pole discretization scheme A.

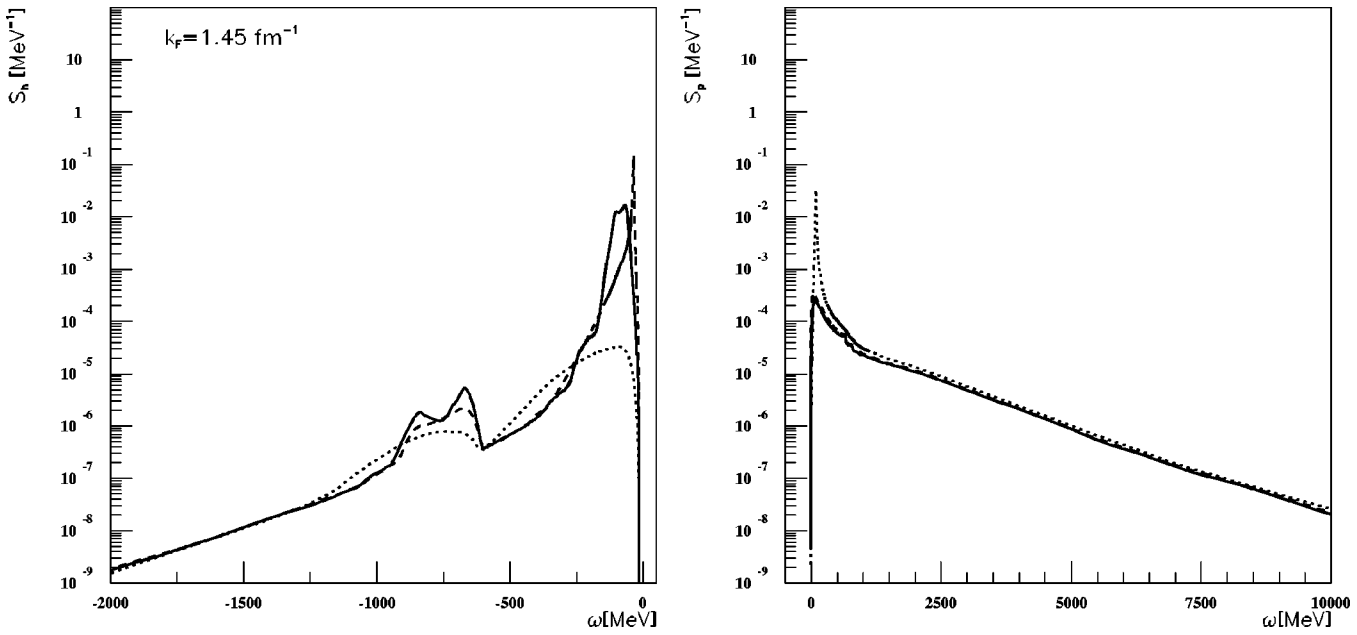

FIG. 15. The energy dependence of the spectral functions obtained using the full Reid 93 interaction, at $k_F=1.45$ fm^{-1}, obtained using discretization scheme A. The full line corresponds to $p=0$, the dashed line to $p=0.8k_F$, and the dotted line to $p=1.7k_F$.

Reid 93 interaction. The right-hand side of this picture shows the momentum-independent tail at high positive energies, caused by the short-range correlations. The slope of this tail is closely related to the hardness of the repulsive core of the interaction, and is therefore highly dependent on the specific interaction used. The tail in the removal domain shown on the left side of the plot is a new feature that is only present in a self-consistent calculation. This tail was also observed in the calculations using a parametrized spectral function [20]. The slope of the tail is independent of the discretization scheme used, only the structures at low energies depend on the specific scheme.

The momentum distribution is presented in Fig. 16. Note that in each iteration both discretization schemes reproduce the correct zeroth-order moment of the continuous hole spectral function. As a consequence, the continuous spectral function and its discrete representation yield the same momentum distribution, which can thus be evaluated as the sum of the strength of the (c) and ($-$) poles for $p<k_F$, and as the strength of the ($-$) pole for $p>k_F$. Surprisingly, even though the discretization schemes are quite different (Fig. 3), they lead to very similar occupation probabilities after convergence. Both schemes yield an occupation at zero momentum of 88%, which is larger than the 83% obtained within a BHF calculation. This observation is consistent with the general observation that a single-pole treatment overestimates the depletion [20]. The strength of the quasiparticle pole at the Fermi momentum equals 0.75, again about 3% larger that its BHF counterpart. At large momenta the occupation probability decreases roughly as an exponential, in conformity with the results obtained from parametrized spectral functions [20].

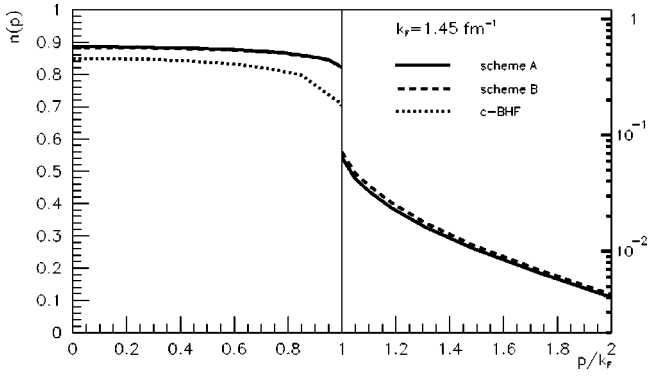

FIG. 16. The occupation probability calculated within the discretization schemes A (full line) and B (dashed line). The left part shows $n(p)$ for hole states on a linear scale; the right part is plotted on a logarithmic scale. For comparison also the qp strength in a continuous BHF calculation is shown for $p<k_F$ (dotted line).

The binding energy can be expressed in terms of the zeroth- and first-order moments of the hole spectral function [54],

$$E_{\rm bind}/A=2\int_{-\infty}^{\epsilon_F}d\omega\int\frac{d\vec{p}}{(2\pi)^3}\quad\left(\frac{p^2}{2m}+\omega\right)S_h(p,\omega). \tag{44}$$

The continuous spectral function and its discrete representation are again equivalent for evaluating the binding energy after convergence. Within the three-pole scheme the expression for the binding energy reads

$$E_{\rm bind}/A=2\int_{p<k_F}\frac{d\vec{p}}{(2\pi)^3}\quad\left(\frac{p^2}{2m}+B_c(p)\right)b_c(p)$$
$$+2\int\frac{d\vec{p}}{(2\pi)^3}\quad\left(\frac{p^2}{2m}+B_-(p)\right)b_-(p). \tag{45}$$

TABLE I. Contributions to the binding energy for $k_F = 1.45$ fm^{-1} (corresponding to a density $\rho_0 = 0.204$ fm^{-3}), using the Reid 93 interaction and discretization scheme A. Nucleons up to a variable threshold momentum p_T are included in the evaluation of the momentum integral. The kinetic and potential energy are also shown, as well as the fraction of the nucleons below p_T.

p_T	$E_{\rm bind}/A$ (MeV)	$E_{\rm kin}/A$ (MeV)	$E_{\rm pot}/A$ (MeV)	ρ/ρ_0
k_F	−8.81	22.41	−31.21	0.86
$2k_F$	−11.72	30.00	−41.72	0.95
$3k_F$	−13.06	38.32	−51.38	0.98
$4k_F$	−13.34	42.31	−55.65	0.99
$5k_F$	−13.35	43.16	−56.52	0.99
∞	−13.36	43.34	−56.69	0.99

In this expression the first term corresponds to the contribution of the quasiparticles to the binding energy. Only nucleons with momenta lower than the Fermi momentum contribute. The second term represents the contribution of the background, to which also high-momentum nucleons can contribute. For very large momenta, the energy of the backward pole approaches $-p^2/2m$ (Fig. 3) and both terms in the integrand tend to cancel. To get some feeling on how important the high-momentum nucleons are, Table I shows results for the binding energy where the integral (45) is evaluated up to a threshold momentum p_T. The corresponding values of kinetic and potential energy are also shown, as well as the fraction of the nucleons with momenta below this threshold. One sees that about 86% of the nucleons are located in states below the Fermi momentum, contributing only 52% of the kinetic energy and 65% of the total binding energy. In order to get convergence for the binding energy, one must at least include nucleons up to $4k_F$. In a fully self-consistent calculation one expects exact particle-number conservation. The last column of Table I shows that the free density is reproduced within 1% accuracy, which is a measure for the numerical accuracy of our calculation.

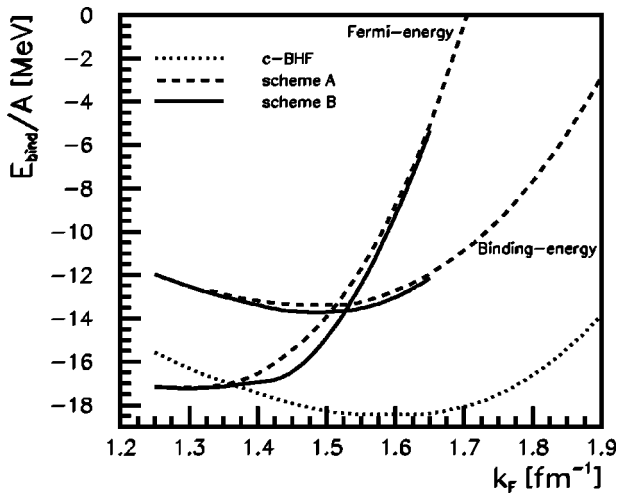

FIG. 17. The binding energy per particle and the Fermi energy, obtained using the full Reid 93 interaction, within discretization schemes A (full line) and B (dashed line). The binding energy in the continuous BHF approach is also shown (dotted line).

TABLE II. Saturation points obtained within a continuous Brueckner scheme and the three-pole schemes A and B, using the Reid 93 interaction. The corresponding value of the nuclear matter compression modulus $K_{\rm nm}$ is also shown.

	$k_{F,0}$ (fm^{-1})	$E_{\rm bind,0}/A$ (MeV)	$K_{\rm nm}$ (MeV)
c-BHF	1.59	−18.48	154
scheme A	1.49	−13.42	177
scheme B	1.48	−13.73	219

The binding energy as a function of Fermi momentum is given in Fig. 17 for the different approaches. Note that the saturation curves are almost identical for discretization schemes A and B. This we take as an indication that on the level of the binding energy the most important requirements for a discrete representation are given by Eqs. (13). When comparing the self-consistent results with the BHF curve, we see that there is an important shift of the saturation point towards smaller densities and smaller binding. The values for the saturation points in Table II were obtained by fitting a fourth-order polynomial in k_F through the calculated points in the region $1.3\ \text{fm}^{-1} < k_F < 1.7\ \text{fm}^{-1}$.

The binding energies calculated within the present scheme have uncertainties of the order of 0.8 MeV caused by various approximations. Firstly, the angle-averaging of the Pauli projection operator can lead to an error of about 0.5 MeV at the larger densities [44,45]. Second, the total error originating from the interpolation procedure and the limited number of points in the various grids is of the order of 0.3 MeV, an estimate based on extensive numerical checks. Finally, errors due to the exclusion of higher partial waves are negligible, as we include partial waves up to $J=3$ in the calculation of the effective interaction. Note that when comparing the Brueckner and self-consistent results, the observed shift in the saturation point is much larger than these uncertainties.

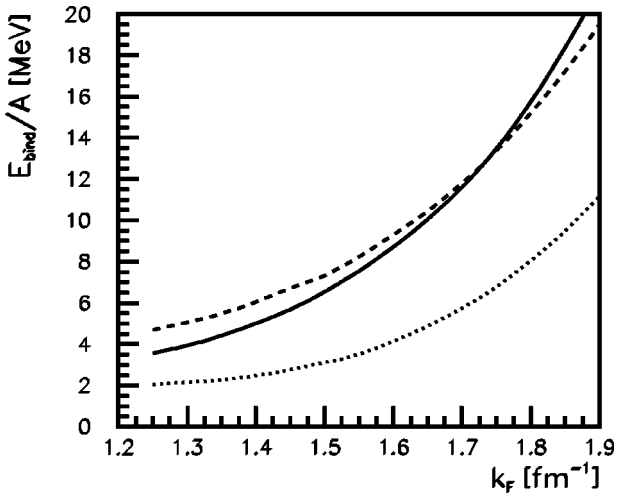

FIG. 18. The binding energy per particle using the reduced Reid 93 interaction. The full line corresponds to the self-consistent calculation using discretization scheme A, the dashed line to the quasiparticle approximation, and the dotted line to a continuous BHF calculation.

A large part of this shift can be attributed to the density-dependent repulsive effect from the inclusion of hh lines in the effective interaction. This was already demonstrated for a quasiparticle calculation with a model interaction [27]. In the self-consistent calculation one gets an additional density dependence by including off-shell propagation in the evaluation of the effective interaction. In order to assess the relative importance of both effects, Fig. 18 shows the saturation curve for a BHF, a quasiparticle, and a self-consistent three-pole calculation (scheme A), using the reduced Reid 93 interaction. Owing to the reduction of the potential no binding is obtained, and one should be careful to generalize the conclusions for the complete interaction. A repulsive effect is seen from the inclusion of hh propagation. This effect increases with the density, as the phase space for hh propagation increases. Full self-consistency leads to an extra density dependency, decreasing the energy at low densities, while increasing it at higher densities.

The nuclear matter compression modulus,

$$K_{\mathrm{nm}}=k_F^2\frac{d^2E/A}{dk_F^2}\bigg|_{k_F=k_{F,0}}, \tag{46}$$

is an important quantity in astrophysics and heavy-ion physics. The values of K_{nm} obtained in the different approaches are also shown in Table II. Although the value of K_{nm} is more sensitive to the specific discretization scheme than the saturation point, a self-consistent treatment seems to lead to an enhancement of the compression modulus. A recent analysis of the giant monopole resonance in heavy nuclei [56] yields an experimental estimate for the compression modulus, $K_{\mathrm{mn}}=210\pm30$ MeV. For the Reid 93 interaction the compression modulus obtained in both self-consistent calculations agrees reasonably well with this value.

Finally, as a check for the thermodynamic consistency of our approach, the Fermi energy for both schemes is shown in Fig. 17. The Hugenholtz–Van Hove theorem states that at the saturation point the binding energy per nucleon equals the Fermi energy [55]. This property is satisfied within less than 1 MeV, which should be compared to the BHF scheme where the Fermi energy is more than 15 MeV below the binding energy at saturation. This observation agrees with recent results by Bozek and Czerski for a separable interaction [57].

VIII. CONCLUSIONS AND OUTLOOK

In this paper a novel method is presented for going beyond the on-shell approximation in the framework of SCGF theory. The method is applied to the nuclear matter problem, using a realistic *NN* interaction. The self-energy and the effective interaction are determined self-consistently, using dressed intermediary propagators that have a spectral width. In order to include the main features of off-shell propagation, the spectral function is approximated by a small set of carefully chosen poles. Two different three-pole discretization schemes are presented. In both schemes, most of the strength is concentrated in a pole located at the on-shell energy, which can be associated with the quasiparticle pole. Two other poles then take care of the background distribution above and below the Fermi energy. The poles and their residues reproduce the correct lowest-order energy-weighted moments of the spectral function, separately for the particle addition and removal domains. Both schemes differ in the way the quasiparticle peak is separated from the background distribution. The final results are to a large extent independent of the chosen discretization scheme.

Results are presented for the Reid 93 interaction. The effective interaction, the self-energy, and the spectral functions are discussed. The discrete approximation leads to shell-like structures in the energy dependence of these quantities. In agreement with the results obtained using a parametrized self-energy, the spectral function has a momentum-independent tail at high positive energies, reflecting the repulsive core of the interaction. Also in the removal domain a momentum-independent tail is found.

In Sec. V the relation between pairing correlations and short-range correlations was investigated. The symmetrical treatment of pp and hh contributions in the effective interaction may lead to pairing instabilities, when one uses projection operators defined with respect to the uncorrelated Fermi sea. The discrete-pole approach does account for the deformation of the Fermi sea, which turns out to be large enough to remove pairing instabilities around the empirical saturation density.

The inclusion of hh propagation to all orders and the use of correct projection operators in the equation for the effective interaction lead to a new density dependence and move the saturation point off the Coester line, towards lower density and less binding. As this density dependence can be different for other potentials it will be important to repeat these calculations for various modern *NN* potentials. This can shed new light upon the role of three-body forces and relativity in the saturation of nuclear matter. Finally it would be of great interest to compare the results of the present discrete-pole approach with those obtained using a parametrized (continuous) spectral function. Qualitatively both methods seem to lead to a number of similar features. For a quantitative comparison both calculations should be performed using the same interaction. This work is in progress.

ACKNOWLEDGMENTS

The authors would like to thank W. Dickhoff for useful discussions. This work was supported by the Fund for Scientific Research-Flanders (FWO-Vlaanderen) and the Research Council of Ghent University.

APPENDIX: TECHNICAL DETAILS

We consider a Green's function having $2M+1$ discrete poles. For $i=1,\ldots,M$ the poles are located at energies $B_i(p)$ below ϵ_F, for all momenta p, and have residues $b_i(p)$. For $i=M+2,\ldots,2M+1$ the poles are located at energies $F_i(p)$ above ϵ_F, for all momenta p, and have residues $f_i(p)$.

The central pole, labeled $i_c=M+1$, is located below ϵ_F for $p<k_F$, crosses the Fermi energy at k_F, and is located above ϵ_F for $p>k_F$, i.e.,

$$f_{i_c}(p)=0 \quad \text{if } p<k_F,$$

$$b_{i_c}(p)=0 \quad \text{if } p>k_F. \tag{A1}$$

The standard angle-averaged Pauli projection operators can be generalized to the multiple-pole case by introducing operators

$$\overline{Q}^{(pp)}_{i_1,i_2}(P,q)=\overline{f_{i_1}(p_1)f_{i_2}(p_2)}=\frac{1}{2}\int dx f_{i_1}(\vec{p}_1)f_{i_2}(\vec{p}_2), \tag{A2}$$

for $i_1 \geqslant i_c$ and $i_2 \geqslant i_c$; and by defining $\overline{Q}^{(pp)}_{i_1,i_2}(P,q)=0$ otherwise. Here $\vec{p}_{1,2}=\vec{P}/2\pm\vec{q}$, and the integration variable x is the cosine of the angle between $\vec{P}$ and $\vec{q}$. Likewise,

$$\overline{Q}^{(hh)}_{i_1,i_2}(P,q)=\overline{b_{i_1}(p_1)b_{i_2}(p_2)}=\frac{1}{2}\int dx b_{i_1}(\vec{p}_1)b_{i_2}(\vec{p}_2), \tag{A3}$$

for $i_1 \leqslant i_c$ and $i_2 \leqslant i_c$; and $\overline{Q}^{(hh)}_{i_1,i_2}(P,q)=0$ otherwise.

The corresponding angle-averaged two-particle energies read

$$\begin{aligned}\overline{E}^{(pp)}_{i_1,i_2}(P,q)&=\overline{F_{i_1}(p_1)+F_{i_2}(p_2)}\\&=\left(\frac{1}{2}\int dx f_{i_1}(\vec{p}_1)f_{i_2}(\vec{p}_2)(F_{i_1}(\vec{p}_1)+F_{i_2}(\vec{p}_2))\right)\\&\quad\times(\overline{f_{i_1}(p_1)f_{i_2}(p_2)})^{-1},\end{aligned} \tag{A4}$$

for $i_1 \geqslant i_c$ and $i_2 \geqslant i_c$, and

$$\begin{aligned}\overline{E}^{(hh)}_{i_1,i_2}(P,q)&=\overline{B_{i_1}(p_1)+B_{i_2}(p_2)}\\&=\left(\frac{1}{2}\int dx b_{i_1}(\vec{p}_1)b_{i_2}(\vec{p}_2)(B_{i_1}(\vec{p}_1)+B_{i_2}(\vec{p}_2))\right)\\&\quad\times(\overline{b_{i_1}(p_1)b_{i_2}(p_2)})^{-1},\end{aligned} \tag{A5}$$

for $i_1 \leqslant i_c$ and $i_2 \leqslant i_c$.

In the quasiparticle approximation the projection operators (A2) and (A3) can be calculated analytically [27]. A multiple-pole calculation requires a numerical evaluation of these quantities, where care must be taken in the angle averaging for the (i_c,i_c) channel, as the corresponding strength functions f_{i_c} and b_{i_c} change rapidly near the Fermi momentum.

For convenience we also introduce operators

$$\overline{Q}^{(\pm)}_{i_1,i_2}(P,q)=\overline{Q}^{(pp)}_{i_1,i_2}(P,q)\pm\overline{Q}^{(hh)}_{i_1,i_2}(P,q) \tag{A6}$$

and energies

$$\overline{E}_{i_1,i_2}(P,q)=\overline{E}^{(pp)}_{i_1,i_2}(P,q)+\overline{E}^{(hh)}_{i_1,i_2}(P,q). \tag{A7}$$

Using this notation and retaining only the principal value in Eq. (26), the integral equation for the reaction matrix R reads

$$\begin{aligned}&\langle q|R_{LL'}(P,\Omega)|q'\rangle\\&\quad=\langle q|V_{LL'}|q'\rangle+\sum_{\alpha L''}\mathrm{P}\int_0^\infty dq''q''^2\langle q|V_{LL''}|q''\rangle\\&\qquad\times\frac{\overline{Q}^{(-)}_\alpha(P,q'')}{\Omega-\overline{E}_\alpha(P,q'')}\langle q''|R_{L''L'}(P,\Omega)|q'\rangle,\end{aligned} \tag{A8}$$

where the channel label α is a shorthand notation for (i_1,i_2).

In a quasiparticle calculation there can only be one singularity for given values of Ω and P. In a multiple-pole calculation each two-particle channel can contain one or more singularities. Multiple singularities within the same two-particle channel arise from the fact that the corresponding two-particle energy is not necessarily a monotonic functions of the relative momentum q.

Consider a channel α with M_α singularities $q_{\alpha i}$, for which

$$\Omega=\overline{E}_\alpha(P,q_{\alpha i}), \quad i=1,\ldots,M_\alpha. \tag{A9}$$

The energy denominator can then be rewritten as

$$\begin{aligned}\frac{1}{\Omega-\overline{E}_\alpha(P,q)}&=\frac{\prod_j(q^2_{\alpha j}-q^2)}{\Omega-\overline{E}_\alpha(P,q)}\frac{1}{\prod_i(q^2_{\alpha i}-q^2)}\\&=\frac{\prod_j(q^2_{\alpha j}-q^2)}{\Omega-\overline{E}_\alpha(P,q)}\\&\quad\times\sum_i\left(\frac{1}{\prod_{j\neq i}(q^2_{\alpha j}-q^2_{\alpha i})}\right)\frac{1}{q^2_{\alpha i}-q^2},\end{aligned} \tag{A10}$$

where an expansion in partial fractions was performed in the last line. In order to further simplify the notation, an additional function A is defined,

$$\begin{aligned}&A^{\alpha i}_{LL'}(\Omega,P,q,q')\\&\quad=q'^2\langle q|V_{LL'}|q'\rangle\frac{\overline{Q}^{(-)}_\alpha(P,q')}{\Omega-\overline{E}_\alpha(P,q')}\frac{\prod_j(q^2_{\alpha j}-q'^2)}{\prod_{j\neq i}(q^2_{\alpha j}-q^2_{\alpha i})}.\end{aligned} \tag{A11}$$

This function is not singular at $q_{\alpha i}$, but has a value determined by the rule of de l'Hôpital,

$$A^{\alpha i}_{LL'}(\Omega,P,q,q_{\alpha i}) = 2q^3_{\alpha i}\langle q|V_{LL'}|q_{\alpha i}\rangle \frac{\overline{Q}^{(-)}_\alpha(P,q_{\alpha i})}{\left.\dfrac{\partial \overline{E}_\alpha(P,q')}{\partial q'}\right|_{q'=q_{\alpha i}}}. \tag{A12}$$

With the help of these additional definition, Eq. (A8) can then finally be rewritten as

$$\begin{aligned}\langle q|R_{LL'}(P,\Omega)|q'\rangle &= \langle q|V_{LL'}|q'\rangle + \sum_{\alpha(ns)}\sum_{L''}\int_0^\infty dq'' q''^2 \langle q|V_{LL''}|q''\rangle \\ &\times \frac{\overline{Q}^{(-)}_\alpha(P,q'')}{\Omega-\overline{E}_\alpha(P,q'')}\langle q''|R_{L''L'}(P,\Omega)|q'\rangle \\ &+ \sum_{\alpha i}\sum_{L''}\mathcal{P}\int_0^\infty dq'' \\ &\times \frac{A^{\alpha i}_{LL''}(\Omega,P,q,q'')\langle q''|R_{L''L'}(P,\Omega)|q'\rangle}{q^2_{\alpha i}-q''^2}. \end{aligned}\tag{A13}$$

In the first integral term we sum over all two-particle channels that have no singularities for given values of Ω and P, and it will be denoted as $\alpha(ns)$. All two-particle channels containing singularities are included in the second term of the sum. The denominator of each of these principal value terms $I_{\alpha i}$ is replaced by a regularized integral $\tilde{I}_{\alpha i}$ with the same value,

$$\begin{aligned}\tilde{I}_{\alpha i} = \mathrm{P}\sum_{L''}\int_0^\infty dq'' \Bigg[&\frac{A^{\alpha i}_{LL''}(\Omega,P,q,q'')\langle q''|R_{L''L'}(P,\Omega)|q'\rangle}{q^2_{\alpha i}-q''^2} \\ &- \frac{A^{\alpha i}_{LL''}(\Omega,P,q,q_{\alpha i})\langle q_{\alpha i}|R_{L''L'}(P,\Omega)|q'\rangle}{q^2_{\alpha i}-q''^2}\Bigg], \end{aligned}\tag{A14}$$

which has a smooth integrand.

The resulting integral equation is turned into a matrix equation by discretizing the momentum variable q. The reaction matrix is then calculated by inversion of a real matrix. Apart from the matrix elements at the N quadrature points, also the matrix elements for the momenta $q_{\alpha i}$ are needed. For a total of $M=\Sigma_\alpha M_\alpha$ singularities, this leads to a matrix dimension of $(N+M)$. For coupled channels the dimensions are doubled.

In this grid of relative momenta the matrix equation for the reaction matrix becomes

$$\begin{aligned}\sum_{L''}\sum_{j=1}^{N+M}\langle q_j|F_{LL''}(P,\Omega)|q_j\rangle\langle q_j|R_{L''L'}(P,\Omega)|q_k\rangle \\ = \langle q_i|V_{L''L'}|q_k\rangle, \end{aligned}\tag{A15}$$

in which the matrix elements of the F matrix are given by $(q_m=1,\ldots,N+M)$

$$\begin{aligned}\langle q_m|F_{LL'}(P,\Omega)|q_n\rangle &= \delta_{LL'}\delta_{\mathrm{mn}} - \sum_{\alpha(ns)} W_n q_n^2 \langle q_m|V_{LL'}|q_n\rangle \frac{\overline{Q}^{(-)}_\alpha(P,q_n)}{\Omega-\overline{E}_\alpha(P,q_n)} \\ &- \sum_{\alpha i} W_n \frac{A^{\alpha i}_{LL'}(\Omega,P,q_m,q_n)}{q^2_{\alpha i}-q_n^2}, \quad q_n=1,\ldots,N \end{aligned}$$

$$\begin{aligned}\langle q_m|F_{LL'}(P,\Omega)|q_n\rangle &= \delta_{LL'}\delta_{\mathrm{mn}} + \sum_{\alpha i}\sum_{k=1}^{N} W_k \frac{A^{\alpha i}_{LL'}(\Omega,P,q_m,q_k)}{q^2_{\alpha i}-q_k^2}, \\ &\qquad q_n=N+1,\ldots,N+M. \end{aligned}\tag{A16}$$

Once the reaction matrix R is constructed, the effective interaction Γ can be calculated. By subtracting Eqs. (26) and (A8) one obtains,

$$\begin{aligned}\langle q|R_{LL'}(P,\Omega)|q'\rangle - \langle q|\Gamma_{LL'}(P,\Omega)|q'\rangle &= i\pi\sum_{\alpha i} q^2_{\alpha i}\frac{\overline{Q}^{(+)}_\alpha(P,q_{\alpha i})}{\left.\dfrac{\partial \overline{E}_\alpha(P,q)}{\partial q}\right|_{q=q_{\alpha i}}}\sum_{L''}\langle q|R_{LL''}(P,\Omega)|q_{\alpha i}\rangle \\ &\times \langle q_{\alpha i}|\Gamma_{L''L'}(P,\Omega)|q'\rangle. \end{aligned}\tag{A17}$$

For convenience yet another vector H is introduced,

$$H_{\alpha i}(P) = \pi q^2_{\alpha i}\frac{\overline{Q}^{(+)}_\alpha(P,q_{\alpha i})}{\left.\dfrac{\partial \overline{E}_\alpha(P,q)}{\partial q}\right|_{q=q_{\alpha i}}} \tag{A18}$$

as well as an additional complex $M\times M$ matrix $\mathcal{M}$,

$$\begin{aligned}\langle q_{\alpha i}|\mathcal{M}_{LL'}(P,\Omega)|q_{\beta j}\rangle \\ = \delta_{\alpha\beta}\delta_{ij} + iH_{\beta j}(P)\langle q_{\alpha i}|R_{LL'}(P,\Omega)|q_{\beta j}\rangle. \end{aligned}\tag{A19}$$

After inversion of this matrix (of small dimension), the complex matrix elements of Γ can be calculated in terms of the reaction-matrix elements

$$\begin{aligned}\langle q|\Gamma_{LL'}(P,\Omega)|q'\rangle &= \langle q|R_{LL'}(P,\Omega)|q'\rangle - \sum_{\alpha i,\beta j}\sum_{L'',L'''}\langle q|R_{LL''}(P,\Omega)|q_{\alpha i}\rangle \\ &\times H_{\alpha i}(P)\langle q_{\alpha i}|\mathcal{M}^{-1}_{L''L'''}(P,\Omega)|q_{\beta j}\rangle \\ &\times \langle q_{\beta j}|R_{L'''L'}(P,\Omega)|q'\rangle. \end{aligned}\tag{A20}$$

[1] H. Müther, A. Polls, and R. Machleidt, Phys. Lett. B **445**, 259 (1999).
[2] H. Müther and A. Polls, Phys. Rev. C **61**, 014304 (2000).
[3] H. Müther and A. Polls, Prog. Part. Nucl. Phys. **45**, 243 (2000).
[4] H.A. Bethe, Rev. Mod. Phys. **8**, 139 (1936).
[5] C.F. von Weizsäcker, Z. Phys. **96**, 431 (1935).
[6] F. Coester, S. Cohen, B. Day, and C.M. Vincent, Phys. Rev. C **1**, 769 (1970).
[7] J.W. Clark, Nucl. Phys. **A328**, 587 (1979).
[8] H.Q. Song, M. Baldo, G. Giansiracusa, and U. Lombardo, Phys. Lett. B **411**, 237 (1997).
[9] B.D. Day and R.B. Wiringa, Phys. Rev. C **32**, 1057 (1985).
[10] A. Akmal, V.R. Pandharipande, and D.G. Ravenhall, Phys. Rev. C **58**, 1804 (1998).
[11] H. Müther, R. Machleidt, and R. Brockmann, Phys. Lett. B **202**, 483 (1988).
[12] J. Carlson, V.R. Pandharipande, and R.B. Wiringa, Nucl. Phys. **A401**, 59 (1983).
[13] A.E.L. Dieperink and P.K.A. de Witt Huberts, Annu. Rev. Nucl. Part. Sci. **40**, 239 (1990).
[14] G.J. Wagner, Rep. Prog. Part. Nucl. Phys. **24**, 17 (1989); in *Nuclear Structure at High Spin, Excitation, and Momentum Transfers*, edited by H. Nann, AIP Conf. Proc. No. 142 (AIP, New York, 1986), p. 220.
[15] G. van der Steenhoven, Nucl. Phys. **A527**, 17c (1991).
[16] L.P. Kadanoff and G. Baym, *Quantum Statistical Mechanics* (Benjamin, New York, 1962).
[17] P. Bozek, Phys. Rev. C **59**, 2619 (1999).
[18] W.H. Dickhoff, Phys. Lett. B **210**, 15 (1988).
[19] C.C. Gearhart, Ph.D. thesis, Washington University, St. Louis, Missouri, 1994.
[20] E.P. Roth, Ph.D. thesis, Washington University, St. Louis, Missouri, 2000.
[21] V.G.J. Stoks, R.A.M. Klomp, C.P.F. Terheggen, and J.J. de Swart, Phys. Rev. C **49**, 2950 (1994).
[22] A.L. Fetter and J.D. Walecka, *Quantum Theory of Many-Particle Sysytems* (McGraw-Hill, New York, 1971).
[23] K.A. Brueckner, C.A. Levinson, and H.M. Mahmoud, Phys. Rev. **95**, 217 (1954).
[24] K.A. Brueckner and C.A. Levinson, Phys. Rev. **97**, 1344 (1955).
[25] K.A. Brueckner, Phys. Rev. **97**, 1353 (1955).
[26] J.D. Jeukenne, A. Lejeune, and C. Mahaux, Phys. Rep. **25**, 83 (1971).
[27] A. Ramos, A. Polls, and W.H. Dickhoff, Nucl. Phys. **A503**, 1 (1989).
[28] A. Ramos, W.H. Dickhoff, and A. Polls, Phys. Lett. B **219**, 15 (1989).
[29] B.E. Vonderfecht, W.H. Dickhoff, A. Polls, and A. Ramos, Nucl. Phys. **A555**, 1 (1993).
[30] F. de Jong and H. Lenske, Phys. Rev. C **56**, 154 (1997).
[31] K. Amir-Azimi-Nili, H. Müther, L.D. Skouras, and A. Polls, Nucl. Phys. **A604**, 245 (1996).
[32] H. Müther and L.D. Skouras, Phys. Lett. B **306**, 201 (1993).
[33] H. Müther and L.D. Skouras, Nucl. Phys. **A581**, 247 (1995).
[34] Y. Dewulf, D. Van Neck, L. Van Daele, and M. Waroquier, Phys. Lett. B **396**, 7 (1997).
[35] Y. Dewulf, D. Van Neck, and M. Waroquier, Phys. Lett. B **510**, 89 (2001).
[36] Y. Dewulf, Ph.D. thesis, Ghent University, 2000.
[37] H.S. Köhler, Phys. Rev. C **46**, 1687 (1992).
[38] C. Mahaux and R. Sartor, Adv. Nucl. Phys. **20**, 1 (1991).
[39] H. Müther, G. Knehr, and A. Polls, Phys. Rev. C **52**, 2955 (1995).
[40] R.V. Reid, Ann. Phys. (N.Y.) **50**, 411 (1968).
[41] T. Cheon and E.F. Redish, Phys. Rev. C **39**, 331 (1989).
[42] W. Legindgard, Nucl. Phys. **A297**, 429 (1978).
[43] R. Sartor, Phys. Rev. C **54**, 809 (1996).
[44] K. Suzuki, R. Okamoto, M. Kohno, and S. Nagata, Nucl. Phys. **A665**, 92 (2000).
[45] E. Schiller, H. Müther, and P. Czerski, Phys. Rev. C **59**, 2934 (1999); E. Schiller, H. Müther, and P. Czerski, *ibid.* **60**, 059901(E) (1999).
[46] M. Trefz, A. Faessler, and W.H. Dickhoff, Nucl. Phys. **A443**, 499 (1985).
[47] B.E. Vonderfecht, C.C. Gearhart, W.H. Dickhoff, A. Polls, and A. Ramos, Phys. Lett. B **253**, 1 (1991).
[48] W.H. Dickhoff, C.C. Gearhart, E.P. Roth, A. Polls, and A. Ramos, Phys. Rev. C **60**, 064319 (1999).
[49] A. Schnell, T. Alm, and G. Röpke, Phys. Lett. B **387**, 443 (1996).
[50] A. Schnell, G. Röpke, and P. Schuck, Phys. Rev. Lett. **83**, 1926 (1999).
[51] P. Bozek, Nucl. Phys. **A657**, 187 (1999).
[52] M. Baldo, U. Lombardo, E. Saperstein, and M. Zverev, Phys. Lett. B **477**, 410 (2000).
[53] P. Bozek, Phys. Rev. C **62**, 054316 (2000).
[54] D.S. Koltun, Phys. Rev. C **9**, 484 (1974).
[55] N.M. Hugenholz and L. Van Hove, Physica (Utrecht) **24**, 363 (1958).
[56] J.P. Blaizot, J.F. Berger, J. Dechargé, and M. Girod, Nucl. Phys. **A591**, 435 (1995).
[57] P. Bozek and P. Czerski, Eur. Phys. J. A **11**, 271 (2001).